The Impact of Pre-Salt Rift Topography on Salt Tectonics: A Discrete-Element Modelling Approach

*Leonardo M. Pichel[1,2], Emma Finch[1], Rob L. Gawthorpe[2]

[1] School of Earth and Environmental Sciences, University of Manchester, Manchester

[2] Department of Earth Science, University of Bergen, Bergen, Norway

Corresponding author: Leonardo M. Pichel (leonardo.munizpichel@manchester.ac.uk)

Key Points:

- Pre-salt rift structures (horst and tilted blocks) generate base-salt relief acting as a major control on salt deformation
- Variable base-salt slope, step height and connectivity between salt sub-basins affect the kinematics of salt-related deformation
- Models present cross-sectional evolution related to complex structural distribution related to salt flux variations over base-salt relief

Abstract

Gravity-driven salt tectonics along passive margins is commonly depicted as domains of updip extension and downdip contraction linked by an intermediate, broadly undeformed zone of translation. This study expands on recently published physical models by applying discrete-element modelling to demonstrate how salt-related translation over pre-salt rift structures produce complex deformation and distribution of structural styles in translational salt provinces. Rift geometries defined by horsts and tilted fault-blocks generate base-salt relief affecting salt flow, diapirism and overburden deformation. Models show how flow across pairs of tilted fault-blocks and variably-dipping base-salt ramps associated with pre-salt faults and footwalls produce abrupt flux variations that result in alternation of contractional and extensional domains. Translation over tilted fault-blocks defined by basinward-dipping normal faults results in wide, low amplitude inflation zones above footwalls and abrupt subsidence over steep fault-scarps, with reactive diapirs that are squeezed and extrude salt as they move over the fault. Translation over tilted-blocks defined by landward-dipping faults produces narrow inflation zones over steep fault-scarps and overall greater contraction and less diapirism. As salt and cover move downdip, structures translate over different structural domains, being inverted and/or growing asymmetrically. Models present, for the first time, a detailed evolution of these systems in cross-section and demonstrate the effects of variable pre-salt relief, salt sub-basin connectivity, width and slope of base-salt ramps. Results are applicable to syn- and post-rift salt basins; ultimately, improving understanding of the effects of base-salt relief on salt tectonics and working as a guide for the interpretation of complex salt deformation.

1. Introduction

Gravity-driven salt-related deformation on passive margins is commonly depicted as kinematically-linked domains of updip extension and downdip contraction connected by an intermediate, broadly undeformed zone of translation (Fig.1a) (Rowan et al., 2000; 2004; Hudec and Jackson, 2004, 2007; Brun and Fort, 2011; Quirk et al., 2012; Jackson et al., 2015). More recent studies (Dooley et al., 2017; Dooley and Hudec, 2017; Pichel et al., 2018) have shown that this structural zonation represents a simplified view of regional salt tectonics and other factors exert a significant effect on the variability of structures developed in space and time. Salt behaves as a viscous fluid over typical geological strain-rates (e.g. Gemmer et al., 2004; Jackson and Hudec, 2017), consequently being sensitive to the geometry of the surface it flows across (Dooley et al., 2017; 2018; Pichel et al., 2018). Therefore, a significant factor which should be considering when examining salt flow and the subsequent development of salt structures is pre-salt topography (Fig. 1b) (Dooley et al., 2017; Pichel et al., 2018).

Late syn-rift to early post-rift salt basins commonly present variable salt thickness and base-salt relief as salt is deposited over a topography inherited from a previous rift phase (post-rift salt) or formed during salt deposition (syn-rift salt). In most cases, salt basins are hybrid, with salt being post-rift landward and syn-rift basinward as rifting propagates towards the embryonic oceanic spreading centre, such as in South and Central Atlantic basins (Rowan 2014; Rowan 2018; Tari et al., 2017). Examples of early post-rift salt basins with significant pre-salt relief include the hydrocarbon-prolific Gulf of Mexico (Peel 1995; Rowan et al., 1995; 2004; Hudec et al., 2013; Dooley and Hudec, 2017) and South Atlantic basins (Mohriak et al., 1995; Hudec and Jackson 2004; Jackson et al., 2008; Davison et al., 2012; Quirk et al., 2012;

Jackson et al., 2015a,b). Late syn-rift salt basins, however, e.g. Nova Scotia (Ings and Shimmeld 2006; Albertz et al., 2010; Deptuck and Kendell, 2017), Morocco and Mauritania (Tari et al., 2000; 2003, 2017; Tari and Jabbour, 2013) are associated with more extreme variations of initial salt thickness both within and across grabens (Jackson and Hudec, 2017).

Where basement fault throw is larger than salt thickness, salt basins are separated into sub-basins that evolve independently (Jackson and Hudec, 2017). In intermediate scenarios (i.e. late syn- and early post-rift salt), lateral flow between sub-basins occurs but pre-salt topography disrupts and limits downdip translation (Jackson and Hudec, 2017). Early physical models simulated progradation over stepped (Ge et al., 1997) and syn-rift salt basins (Adam and Krezsek, 2012), providing important insights into the effects of differential loading and their long-lived evolution. These studies, however, did not address the significant effects of early gliding and downdip translation associated with post-rift thermal subsidence and basinward tilting typical of passive margins (Rowan et al., 2004; Peel 2014; Jackson et al., 2014). Recent analogue models (Dooley and Hudec, 2017; Dooley et al., 2017, 2018) have demonstrated how translation across pre-salt relief promotes salt flux variations that result in complex, multiphase salt tectonics (Fig. 1b). These pioneering studies focus on the plan-view evolution of these systems and do not analyse the cross-sectional variations in diapirism style (i.e. reactive, passive and active, (Vendeville and Jackson, 1992a; Hudec and Jackson, 2007) through time and space relative to changes in salt flow and overburden deformation patterns.

In this study, we employ a Discrete-Element Modelling (DEM) approach (Finch et al., 2003, 2004; Schöpfer et al., 2006; Abe and Urai, 2012; Pichel et al., 2017) to investigate translation across semi-isolated salt sub-basins. These sub-basins are associated with horst and tilted fault-blocks, which define more realistic base-salt geometries along rifted passive margins than previous studies (Dooley et al., 2017). This approach allows for analysis of how salt flux and overburden deformation are affected by: 1) the presence of two pre-salt structures (i.e. tilted fault-blocks), 2) base-salt ramps with different slopes and orientation according to the geometry of the underlying pre-salt structures, and 3) variable base-salt step height and connectivity between salt sub-basins. These results are important for understanding the evolution of salt-related deformation and to guide interpretation of complex salt and supra-salt structural framework along passive margins salt basins. Furthermore, results show that salt and supra-salt geometries can be directly linked to pre-salt structures and, therefore, recognition of similar structural patterns on continental margins can aid in the identification of (usually) poorly-imaged pre-salt structures.

2. Method and Models Design

While physical models provide invaluable insights into the 3D geometry, timing and planform sequential evolution of structures (Vendeville and Jackson, 1992; 1995; Dooley et al., 2007; 2015; Ferrer et al., 2012; 2017), they demand a significant amount of time, space and investment (Pichel et al., 2017). Numerical models based on continuum methods, such as finite-element modelling (FEM), have proved very useful in understanding the dynamics of salt flow, allowing more numerical control and realistic stress-strain quantification (Gemmer et al., 2004; Gradmann et al., 2009; Albertz et al., 2010; Weijermars et al., 2015). They are not able, however, to reproduce spontaneous, realistic fault localization and propagation in the cover, which is critical to understand the kinematic and structural style of minibasins and diapirs in areas affected by regional stresses. Thus, FEM cannot reproduce accurately the development of reactive diapirs driven by regional extension

(Vendeville and Jackson, 1992a), which are important in the settings focus of this study.

As with any other modelling technique, DEM has advantages and disadvantages (Botter et al., 2014). DEM limitations regard the need of meticulous calibration of particle parameters (Botter et al., 2014) and, because of its discontinuous nature, the (Newtonian) viscous behaviour of salt is approximated (Abe and Urai, 2012; Pichel et al., 2017). Nevertheless, the method allows a good first-order approximation of viscous salt flow at a regional scale that can be used to analyse various aspects of salt tectonics and diapirism driven by regional stresses (Pichel et al., 2017). The advantages of DEM are: 1) scaling is not a restriction; 2) models are easily reproducible, not requiring constant and complex re-meshing; 3) they provide higher resolution and analysis of small-scale deformation within the overburden; and, 4) they promote more realistic, natural development and evolution of faults and folds in the sedimentary cover than other numerical techniques (Finch et al., 2003; 2004; Pichel et al., 2017). The DEM technique used in this study derives from the Lattice Solid Model (Mora and Place 1993, 1994; Place et al. 2002) and the Particle Dynamics Method (Finch et al., 2003). The technique has been extensively applied to model dynamic evolution of geological systems (Donzé et al., 1994; Place et al., 2002), including faulting and folding processes (Finch et al., 2003, 2004; Hardy and Finch, 2005, 2006, 2007; Schöpfer et al., 2006; Deng et al., 2017; Finch and Gawthorpe, 2017); viscous flow associated with development of boudinage structures (Abe and Urai, 2012) and salt diapirism (Pichel et al., 2017).

The rock mass is treated as an assemblage of circular elements linked by breakable elastic springs through a ‘repulsive-attractive’ force obeying Newton's Laws of motion (Mora and Place, 1993, 1994; Finch et al., 2004; Hardy and Finch, 2006). The relative strength of each assemblage is defined by its breaking separation, so particles remain bonded until this threshold is exceeded (Donzé et al., 1994; Finch et al., 2004). The motion of particles is assumed to be frictionless and cohesionless with elasto-plastic and ductile behaviour for the overburden and salt, respectively (Finch et al., 2003; Hardy and Finch, 2007, Pichel et al., 2017). The elements have four radii of 0.2, 0.3, 0.4 and 0.5 units and are randomly distributed to reduce failure in preferential orientations within the matrix. A viscous term (v) is added to counteract the elastic behaviour and buildup of kinetic energy within a closed system, enabling its stabilization, which makes it ideal for studying quasi-steady tectonic processes (Finch et al., 2004; Pichel et al., 2017).

Forces are resolved in the x and y directions and elements are also subjected to gravitational forces, F_g. The equations that define the inter-relationship of all forces acting on the DEM are:

$$F_x = F_{i,n} - v\dot{x} \qquad (1)$$

$$F_y = F_{i,n} - v\dot{y} + F_g \qquad (2)$$

Where $F_{i,n}$ corresponds to the total elastic force acting on a particle, v represents the dynamic viscosity and $\dot{x}$ and $\dot{y}$ correspond to the velocity of the particle.

In order to make DEM applicable to regional-scale salt tectonics, the properties of elements representing salt are adjusted so they behave macroscopically as a viscous-plastic material. This is achieved by assigning them a negligible breaking separation so their motion is entirely controlled by the viscosity and gravity of the system (Pichel et al., 2017). This does not reproduce the entire range of salt-related mechanical processes; but, based on stress-strain responses obtained by compressional tests (Pichel et al., 2017, fig. 2), works as a good first-order approximation for regional studies. These tests show that a separation threshold of 0.001 of particles assigned to salt produces a linear, horizontal response with negligible elastic component. This response is representative of ductile viscous-plastic materials, and notably similar to curves produced by physical (Spiers et al., 1990) and numerical (Li and Urai, 2016) experiments of salt deformation.

The model salt viscosity is 1.1 x10^{9} Pa.s, which is lower than its real viscosity (10^{17}–10^{20} Pa s – Gemmer et al., 2004; Jackson and Hudec, 2017). However, as models of salt flow involve solid-state creep, negligible inertial forces and Reynolds number (Re <<1), geometric similarity ensures dynamic and kinematic similarity despite numerical parameters not being identical to the real world (Weijermars and Schmeling, 1986; Weijermars et al., 1993; Schultz-Ela et al., 1993; Pichel et al., 2017). The Poisson's ratio (v) for 2D DEM models is 0.33 and the Young Modulus (E) of the elasto-plastic overburden is of 6.75 GPa. These values are similar to previous studies of salt tectonics (Pichel et al., 2017), and in the range of natural examples of salt and an overburden composed of semi-consolidated siliciclastic rocks or marls (Johnson and DeGraff, 1988; Liang et al., 2007). For a full and more detailed description of scaling of parameters and equations governing DEM, see Mora and Place (1994), Finch et al., (2004); Hardy and Finch (2005, 2006) and Pichel et al., (2017).

We present three models where the impact of typical pre-salt rift structures on early-stage salt tectonics, i.e. gliding over a regionally dipping salt detachment (Rowan et al., 2004; Peel 2014b), is tested: i) Model A: horst-block (Fig. 2a), ii) Model B: tilted fault-blocks with basinward-dipping normal faults (Fig. 2b), and iii) Model C: tilted fault-blocks with landward-dipping normal faults (Fig. 2c). Salt-related gliding and viscous shear drag within the salt are associated with the process of post-rift thermal subsidence and consequent margin tilt (e.g. Rowan et al., 2004; Peel 2014; Pichel et al., 2018). These processes are reproduced in the models by simulating salt-related translation over a 3° basinward-dipping salt detachment (Fig. 2), which is in agreement with the slope of salt detachment on passive margins (Tari et al., 2003; Peel 2014) and previous models (Brun and Fort, 2011; Dooley et al., 2007; Dooley et al., 2015; 2017; Pichel et al., 2017).

For simplicity and general applicability, we do not simulate syn-kinematic sedimentation and assume a homogeneous overburden underlain by a salt interval with densities of, respectively, 2.3 g cm^{-3} and 2.16 g cm^{-3}. These values concur with nature and previous physical and numerical analogues (Gemmer et al., 2005; Ings and Shimmeld, 2006; Dooley et al., 2009, 2012, Albertz and Ings, 2012; Gradmann and Beaumont, 2016). The maximum and minimum salt thicknesses for each model are, respectively, 2.1 km and 750 m due to gradual thinning of the salt onto pre-salt structural highs. The pre-kinematic overburden has a constant thickness of 0.9 km. As both thickness and density ratios of models and natural examples are similar, stresses in the overburden are dynamically scaled (Weijermars et al., 1993, Pichel et al., 2017).

The horst model (A) presents a setting similar to that modelled in Dooley et al. (2017) to illustrate how the approach reproduces the expected kinematics and strain-distribution associated with salt-related translation across pre-salt relief. In addition, we evaluate the sequential evolution of structures in cross-section, something not analysed by Dooley et al. (2017). The model comprises a single central horst block (8 km wide and 1.35 km high) defined by a landward- and a basinward-dipping (50°) normal fault at its updip and downdip edges, respectively (Fig. 2a).

The tilted fault-block models (B and C) display novel scenarios where we evaluate the influence of steep and gentle base-salt ramps defined, respectively, by syn-rift normal faults and their footwalls (Fig. 2b-c). These models comprise a pair of equidimensional, 10 km wide asymmetric fault-blocks with a 50°-dipping normal fault and a gentle (7.5°) footwall. The maximum pre-salt structural relief occurs at the footwall crest and is 1.35 km with respect to the base of the model (Figs 2b-c). In an additional set of experiments, we evaluate the effects of variable structural relief and connectivity between salt sub-basins on salt flow and overburden deformation for the tilted fault-block models. The footwall crest height is set at 1.2, 1.5, 1.8 and 2.1 km (Models B1B4 and C1-C4, fig. 2d-e) (Table 1), whereas its location relative to model boundaries remains fixed. Particles within the salt and overburden are subject to gravitational settling in order to ensure mechanical stability, producing an initial subtle monoclinal relief at the edges of pre-salt structures (Fig. 2). The monocline and cover outer-arc extension are typical geometries associated with end of rift stretching and syn-depositional salt flow (Duffy et al., 2013; Rowan 2014; Jackson and Hudec, 2017).

Models are run for 5 million time-steps, which are scaled to 10 Ma in order to simulate translation rates and magnitudes compatible to the early-stage salt-related deformation typical of passive margins (Rowan et al., 2004; Jackson and Hudec, 2005; Peel 2014; Pichel 2018). Thus, a total of 7.5 km of downdip translation is produced by moving end-walls basinward at an equal and constant rate of 0.75 mm/year, equivalent to a strain-rate in the order of 10^{-16} s^{-1}, within the typical range of salt tectonics along passive margins (Rowan et al., 2004; Jackson and Hudec, 2017; Pichel et al., 2018). The boundaries of the models are not shown because these are not relevant in this study, which focuses on deformation above pre-salt syn-rift structures.

3. Salt flow across a Horst-block (Model A)

This model presents a cross-sectional sequential evolution of a system affected by salt-related translation across a rigid and isolated pre-salt horst block (Fig. 3). As the salt and overburden move downdip across the horst, salt flux varies at its edges generating localized zones of deformation that change and expand through time as strain increases. Salt flux variations occur in response to local changes in the cross-sectional area of flow as the entire system moves across the pre-salt rift topography and the associated base-salt ramps, as shown in physical models (Fig. 1b) (Dooley et al., 2017).

During the first 4 Myr, minor salt inflation and cover uplift occur over the horst's updip edge reversing the initial drape-fold geometry (Fig. 2a and 3a-b). As the salt is originally thicker updip of the horst, the amount of salt being fed towards its updip edge is higher than the amount of salt leaving it, resulting in salt surplus and inflation. As salt becomes progressively thicker over this landward-dipping edge of the horst, it begins to accelerate and extend over the horst's gentle and wide basinward-dipping crest causing the extensional zone to expand (Fig. 3b).

Conversely, the amount of salt moving over the horst's downdip edge is significantly less than the amount moving out, producing salt deficit and subsidence of the cover (Fig. 3a-b). This amplifies the initial monocline formed prior to translation (see section 2, fig. 2a), generating an extensional zone at the top of, and a contractional zone at the base of the basinward-dipping pre-salt fault. These zones are defined, respectively, by an extensional and a contractional hinge (*sensu* Dooley et al., 2017) at the edges of the monocline (Fig. 3a-b). The extensional zone is characterized by reactive diapirism and predominantly basinward-dipping listric normal faults in the cover with salt rollers in their footwalls (Fig. 3a-b). The downdip contractional zone is defined by basinward-verging thrusts, salt inflation, cover uplift and folding with related outer-arc extension (Fig. 3a-b). During the first 2 Myr, a symmetric reactive diapir (1_R, fig. 3a) forms at the top of the basinward-dipping pre-salt fault, a point that defines a base-salt extensional hinge where extension is greater (Fig. 3a). In the next 2 Myr, new reactive diapirs (2_R and 3_R, fig. 3b) form at this point as the earlier one (1_R, fig. 3b) moves downdip. During this stage (at 4 Myr), an imbrication of thrusts starts to impose differential structural loading driving additional salt attenuation at base of the pre-salt fault and inflation downdip (Fig. 3b).

With continued translation, salt flux variations are amplified increasing updip inflation and cover uplift over the horst's landward-dipping edge and salt depletion and cover subsidence on its basinward-dipping edge (Fig. 3c). Updip inflation results in development of a broad salt anticline over the landward-dipping fault, whereas downdip, over the basinward-dipping fault, deformation becomes progressively more complex and inversion of previous structures occurs (Fig. 3b-c). Wide reactive diapirs (4_R and 5_R, fig. 3c) originate at the top of the basinward-dipping fault (i.e. base-salt extensional hinge). Immediately downdip of this fault, extensional structures originally formed near its crest move across a contractional hinge at the base of the fault and are inverted (Fig. 3a-c). Normal faults are reactivated as thrusts with minor salt flow in their hangingwall, whereas reactive diapirs (1_R and $2_{R,}$ fig. 3b) are squeezed (1_S and 2_S, fig. 3c). Progressive subsidence over the horst's downdip fault and differential loading by thrusting downdip leads to substantial thinning of the salt locally reducing translation and downdip inflation (Fig. 3c).

At 8 Myr (Fig. 3d), continuous inflation over the horst’s updip edge results in increased thickening and widening of the salt anticline. The anticline moves partially over the wide and gentle basinward-dipping horst’s crest and, as a consequence, it undergoes asymmetric and hybrid growth. This hybrid deformation is characterized by an active diapir (6_A, fig. 3d) that uplifts and pierces its cover on the updip limb of the anticline, located above the horst’s updip edge, while its downdip limb widens and extends as it moves over the horst’s crest and collapses (Fig. 3d). At the horst’s downdip edge, the wide reactive diapir (4_R, fig. 3d) moves across the pre-salt basinward-dipping fault, being squeezed and rising further (4_S, fig. 3d). Continuous salt depletion over this fault reduces lateral flow and, consequently, a primary weld forms downdip of the horst causing contraction to migrate landward over the pre-salt fault (Fig. 3d).

By the end of the experiment, the broad anticline formed over the horst’s updip edge has translated completely over the horst’s crest (Fig. 3e). This inflated salt body undergoes further extension, being pierced by small reactive diapirs while a new, smaller anticline forms updip, over the landward-dipping fault (Fig. 3e). These geometries and kinematics are similar to the patterns observed in physical models (Fig. 1b) (Dooley et al., 2017). Over the basinward-dipping fault, as salt is dramatically thinned between diapirs (4_S and 7_S, fig. 3e), the two salt sub-basins defined by the horst block become partially disconnected. As a consequence, the reactive diapir (5_R, fig. 3d) formed at the top of the fault cannot subside and is instead squeezed (5_S, fig. 3e) over the earlier formed diapirs. This results in a set of basinward-leaning squeezed diapirs with overturned flanks and, occasionally, secondary welds (2-4_S and 7_S, fig. 3e).

4. Pre-salt Tilted Fault-Blocks with Basinward-dipping Normal Faults (Model B)

This model simulates a more complex scenario where salt and overburden translation is affected by a pair of tilted pre-salt fault-blocks (A and B), defining gentle landward-dipping (footwalls A and B) and steep basinward-dipping base-salt ramps (faults A and B, fig. 2b and 4). During the first 2 Myr, mild inflation and overburden uplift occurs at the updip edge of footwall A because the cross-sectional area of salt arriving there is greater than that leaving producing salt surplus (Fig. 4a). The effect is less evident over footwall B because basinward movement of the system is partially buttressed by Fault-block A, although deformation over Fault B is greater due to the unimpeded basinward advance beyond the fault. There, a 3 km wide zone of extension and reactive diapirism (1_R, fig. 4a) occurs at the crest of Fault B, passing to salt thinning and cover subsidence above the fault, and inflation further downdip.

During the following 2 Myr (Fig. 4b), the inflation zone over footwall A widens and subsidence over Fault B increases. The earlier reactive diapir (1_R) rises further due to increased extension, and new extensional faults and a reactive diapir (2_R, fig. 4b) form immediately updip while earlier-formed normal faults are inverted as they move across fault B (Fig. 4a-b). As translation continues, the inflation/contraction zone associated with footwall A widens and salt flux variations become greater over Fault A and footwall B (Fig. 4c). This results in mild subsidence over Fault A with normal faulting at its crest and reverse faults over its base and into footwall B (Fig. 4c). The first reactive diapir (1_R, fig. 4a-b) emerges and starts to grow passively as it moves over the extensional hinge at the crest of Fault B (1_P, Fig. 4c). At the same time, salt continues to thin over Fault B while new thrusts form immediately downdip, at its base, where salt flow decelerates (Fig. 4c).

By 8 Myr (Fig. 4d), continuous inflation and contraction over footwall A results in the development of two salt anticlines while subsidence coupled with updip extension and downdip contraction are amplified over fault A. Extension is characterized by normal faulting and reactive diapirism over its crest, whereas contraction is associated with reverse faulting and active diapirism at the base of the fault and inflation over footwall B (Fig. 4d). This leads to the development of a hybrid diapir (4_H, fig. 4d), which rises reactively by extension on its updip flank, located above the footwall crest of fault A; and by active diapirism, flank upturn and contraction on its downdip flank over the base of the fault. The diapir (4_H, fig. 4d) is triangular in shape, being characterized by inward-dipping and younging normal faults and a sub-regional and sub-horizontal extended roof on its updip flank, a geometry characteristic of reactive diapirs formed by extension (*sensu* Vendeville and Jackson, 1992a). Its downdip flank, however, presents a typical upturned and uplifted flap geometry denoting active rise (c.f. Schultz-Ela et al., 1993; Hudec and Jackson, 2007).

Over fault-block B, a wide reactive diapir (3_R, fig. 4d) nucleates at the edge of the previously inflated salt body as it extensionally collapses when it reaches the extensional hinge at the footwall crest of fault B. The earlier passive (1_P) and reactive (2_R, fig. 4c) diapirs move across this fault and are squeezed and rotated basinward ($1\text{-}2_S$, Fig. 4d). The initial diapir (1_S, fig. 4d) is almost completely pinched-off extruding salt from its crest to produce a small salt sheet (Sh_1, fig. 4d).

By 10 Myr (Fig. 4e), the landwardmost anticline amplifies over footwall A as it approaches the footwall crest, whereas the anticline immediately downdip moves over the extensional hinge on Fault A’s footwall crest and is extended by a series of landward-dipping normal faults. The earlier hybrid diapir (4_H, fig. 4e) moves across Fault A, rising and upturning further its flanks as it is squeezed over footwall B. The anticline located immediately downdip is also further contracted and amplified as it translates over footwall B (Fig. 4e). A new reactive diapir (6_R, fig. 4e) forms on the downdip limb of this anticline as it reaches the extensional hinge on the footwall crest of Fault B. The earlier-formed reactive diapir (3_R, fig. 4d) moves over the contractional hinge at the base of Fault B where it is squeezed and rises further (3_S, fig. 4e). Due to their greater width (1.5-3 km), diapirs 2_S and 3_S do not weld like the oldest, narrower (< 1 km) diapir (1_S, fig. 4e), which remains broadly unchanged as it lost its connection with the source-layer at an earlier stage (Figs 4d-e).

5. Pre-Salt Tilted Fault-Blocks with Landward-dipping Normal Faults (Model C)

During the first 2 Myr of this model, deformation is focused away from the underlying structures in the form of small reverse faults updip, and normal faults and salt rollers downdip (Fig. 5a). This occurs because Fault A defines a steep base-salt step that dips against the flow direction, buttressing downdip flow and enhancing updip contraction; whereas the basinward-dipping footwall B favours downdip gliding and extension (Fig. 5).

During the following 2 Myr, continued buttressing of salt flow against Fault A results in additional inflation and development of a salt anticline above it (Fig. 5b). Gliding over footwall B results in increased extension and development of reactive diapirs

(Fig. 5b). By 6 Myr (Fig. 5c), progressive translation and increased salt inflation over Fault A widens the updip anticline, which moves partially over the footwall crest of Fault A. This produces minor flux variations over footwall A and, consequently, mild updip extension of the anticline and downdip shortening, which is associated with the development of a wide zone of mild inflation as flow is buttressed against Fault B (Fig. 5c).

By 8 Myr, both zones of inflation formed over faults A and B amplify, becoming wider and affected by outer-arc stretching (Fig. 5d). A reactive diapir (1_R, fig. 5d) forms above the inflated salt over Fault B as this zone expands and moves over the extensional hinge at Fault B's footwall crest, where it is influenced by gliding and extension above footwall B. The anticline formed over Fault A, however, is only locally extended by outer-arc stresses because downdip translation over footwall A is buttressed by fault-block B producing greater inflation and contraction over the entirety of fault-block A (Fig. 5d). By the end of the experiment, both anticlines thicken and widen, extending asymmetrically on their basinward flanks as they move over the extensional hinges on the footwall crest of both faults (Fig. 5e). The reactive diapir (1_R, fig. 5e) leaves the footwall crest of Fault B and a new reactive diapir (2_R, fig. 5e) nucleates immediately updip. The updip, larger anticline is asymmetrically extended and affected by a reactive diapir (3_R, fig. 5e) as the anticline's crest moves beyond the buttressing Fault A.

6. Effects of step height and connectivity between sub-basins

In this set of experiments, we evaluate the effects of pre-salt structural relief and the associated variable salt thickness and connectivity across sub-basins by varying the height of the fault scarp in four increments: 1.2, 1.5, 1.8, and 2.1 km (Figs. 6a-d and

7a-d). The location of the footwall crest and slope of base-salt ramps remain constant so the width of the pre-salt structures and base-salt ramps, and the overall salt volume vary. As base-salt structural relief increases, the salt thickness connecting the sub-basins decreases, so that the salt is completely separated in the cases with the largest structural relief (models B4 and C4, figs. 6d and 7d). In this section, we present focused views from the centre of these experiments to improve visualization and comparison of final geometries (Figs. 6 and 7).

In both cases of sub-basins defined by basinward- and landward-dipping faults, salt flux mismatches are directly proportional to the base-salt relief and associated salt thickness contrasts across sub-basins. For basinward-dipping pre-salt faults (Fig. 6), an increase in the footwall crest height results in greater buttressing and salt inflation over the footwall (i.e. base-salt landward-dipping ramp); and greater salt thinning above the fault (i.e. base-salt basinward-dipping ramp) (Fig. 6a-c). Flux mismatches are, therefore, enhanced where salt is thinner over fault crests (Fig. 6). The magnitude and width of inflation increase progressively from Model A (1.2 km fault scarp) to Model D (2.1 km fault scarp, fig. 6). As cover subsidence and salt thinning are also intensified over the larger fault scarps, the width of associated extensional and contractional zones, number of normal faults and intensity of reactive diapirism increase from Models A through B and C (1.2, 1.5 and 1.8 km of fault scarp height respectively, figs. 6a-c). The locus of maximum subsidence remains closer to the base of the fault scarp as the pre-salt step height increases and, consequently, the connectivity between sub-basins decreases (Fig. 6).

These relationships do not completely apply for Model B4 (Fig. 6d), where salt sub-basins are initially completely disconnected. In this scenario, extension and contraction are more localized and divided into two segments (Fig. 6d). A narrow zone of extension forms due to gliding and salt thinning over the fault, passing immediately downdip to a wider area of contraction above the base of the fault and the adjacent footwall (Fig. 6d). Immediately updip of this, another pair of extensional and contractional domains develop as a salt sheet advances from the updip sub-basin over the thinned salt portion of the downdip one (Fig 6d). Gradual translation and inflation over the footwall crest allows salt to build enough gravitational instability and velocity, causing it to advance by thrusting over the extensionally thinned salt in the downdip sub-basin (Fig. 6d). This results in a greater amount of contraction than extension at this location (Fig. 6d). The salt is initially isolated by footwall topography, therefore, not being able to flow continuously from the updip sub-basin onto the downdip one, which results in profound salt attenuation and weld development over the fault (Fig. 6d). However, once the salt advances over the footwall crest, these initially isolated systems no longer evolve independently and the proximal salt imposes additional structural loading that amplifies salt expulsion and downdip inflation (Fig. 6d).

In landward-dipping pre-salt fault systems, the amount of buttressing is directly proportional to the fault and associated base-salt step heights and differences in salt thickness across sub-basins. As a consequence, the magnitude of salt inflation, overburden contraction and uplift is larger for greater steps (Fig. 7a-c), except in the case of disconnected sub-basins (Fig. 7d). The observed zone of inflation is located progressively further basinward for models with smaller footwall crests, because salt is able to flow more easily across lower relief steps; whereas it remains pinned for a greater time over higher steps (Fig. 7a-d). This results in nucleation of a larger number of reactive diapirs over the inflated salt for models with smaller footwall crests (Fig. 7). Similar to the basinward-dipping faults models (Fig. 6), when the salt sub-basins are initially isolated they evolve independently until the salt inflates enough over the footwall crest so it becomes able to advance basinward over previously thinned strata in the downdip sub-basin (Fig. 7d).

7. Discussion

7.1. Effects of Pre-salt Rift Geometries on Salt Flow and Overburden Deformation

The results of this study improve understanding of how pre-salt structures and associated base-salt relief control salt flow, overburden deformation and distribution of structural styles along passive margins. Realistic rift geometries defined by pre-salt horsts and tilted fault-blocks have been simulated and can be applied to a wide range of basin geometries (Fig. 8). The models do not intend to simulate the entire lateral extent and temporal evolution of salt basins; rather, they focus on a single and important component of their early history, gliding, which is often overlooked due to the structural complexity and limited seismic resolution of deepest supra-salt strata.

The horst-block model (Model A) reproduces a similar dynamic evolution and distribution of structural styles to the physical models of Dooley et al. (2017) (Figs. 1b, 8a and 9a). Salt-related translation promotes variations in the cross-sectional area of salt flow across a pre-salt horst (Fig. 9a). This results in salt surplus and inflation at the horst's landward-dipping updip edge and salt deficit and thinning over its basinward-dipping downdip edge (Fig. 8a and 9a). Continuous flow over the horst's landward-dipping edge results in development of an inflated salt anticline that progressively thickens and widens, eventually moving over the horst's crest where it collapses and extends (Figs. 3 and 8a). Downdip, over the horst's basinward-dipping edge, the zone of salt thinning and cover subsidence is characterized by a monoclinal geometry limited by extension and reactive diapirism over the footwall crest, and contraction and diapir squeezing at the base of the fault (Figs. 3 and 8a). With continued subsidence and deformation above the ramp, salt is significantly thinned pinning downdip movement and promoting updip migration of the contractional zone (Fig. 3d-e). These similarities with recent physical models (c.f. Dooley et al., 2017) and additional details on the cross-sectional evolution of structures demonstrates the capability of the method to simulate differential salt flow, multiphase deformation and diapirism associated with salt flux variations across base-salt relief.

Tilted fault-block models (Figs. 4-7) demonstrate how translation across sets of steep and gentle base-salt ramps associated with syn-rift faults and footwalls result in more complex patterns of diapirism and structural distribution. This occurs because the salt flux varies more frequently and abruptly as it encounters further changes in base-salt relief (Fig. 8b-c and 9b-c). These models also describe how the width and height of pre-salt structures play a key role in controlling the structural style and evolution of these systems (Figs. 6-8).

In models of translation across tilted fault-blocks defined by basinward-dipping normal faults (Model B), wide zones of salt inflation and overburden contraction develop over the gentle landward-dipping base-salt ramps at the footwall of these fault-blocks (Figs. 4 and 9b). This occurs because initial salt thickness decreases towards the footwall crest and, as the system translates, the cross-sectional area of salt arriving at that point is larger than that leaving (Fig. 9b). In contrast, salt flux over basinward-dipping faults that form steep base-salt ramps result in the cross-sectional area of salt arriving at the footwall crest being smaller than that leaving over the fault scarp, where salt was initially thicker (Fig. 9b). This generates a monoclinal zone of subsidence above the fault defined by extension over the footwall crest and contraction over the base of the fault (Figs. 4, 8b and 9b). As translation continues, deformation intensifies with the zone of extension expanding landward and the zone of contraction basinward (Fig. 4). Extensional structures (i.e. normal faults and reactive diapirs) initially formed near the footwall crest (i.e. extensional hinge) translate over the base of the fault scarp where flow decelerates (i.e. contractional hinge), and are rotated, inverted and/or squeezed (Figs. 4, 8b and 9b). Salt anticlines developed above the footwall translate over the footwall crest and become extended and pierced by reactive diapirs (Figs. 4 and 8b). This pattern repeats for each fault-block encountered resulting in more abrupt transitions, overlap and alternation of contractional and extensional domains relative to settings with simpler base-salt relief, e.g. horst blocks (Fig. 8a-b).

When tilted blocks are defined by landward-dipping normal faults (Model C), intense buttressing of salt flow and, thus, greater salt inflation and contraction are observed above the fault (Figs. 5, 8c and 9c). This results in higher-amplitude, but narrower zones of inflation and contraction compared with the basinward-dipping normal fault model (Figs. 8b-c). Additionally, the presence and proximity of two flow buttresses associated with the underlying pre-salt structures results in overall greater magnitudes of shortening and reduced extension and subsidence compared with other models (Figs. 8 and 9c). As translation continues, salt anticlines become progressively wider and thicker, eventually moving across the footwall crest and over the gentle basinward-dipping footwall (Figs. 5 and 8c). As a consequence, the anticlines are asymmetrically extended and pierced by reactive diapirs, with greater magnitude of extension occurring on their downdip flank located over the basinward-dipping footwalls (Fig. 5 and 8c). Moreover, as regional contraction does not favour diapirism as much as extension (Vendeville and Jackson, 1992a; 1994), translation over pre-salt fault-blocks defined by landward-dipping normal faults results in considerably less diapirism than in other settings (Fig. 5 and 8).

Our experiments confirm the hypotheses that pre-salt structures and base-salt topography are responsible for nucleating salt structures by promoting changes in salt flow and overburden deformation patterns (Ge et al., 1997; Dooley et al., 2017; 2018; Deptuck and Kendell, 2017; Pichel et al., 2018) (Figs. 3-5). As translation progresses, the salt structures eventually leave the pre-salt topography where they were triggered, being reactivated downdip by the next pre-salt structure encountered (Figs. 3-5). These early-formed structures act as weakness zones that may be eventually exploited and amplified by later processes such as loading or tectonic reactivation, further complicating the evolution of these systems (Dooley et al., 2018), and our ability to interpret them.

The models reproduce a wide range of diapirism styles (i.e. reactive, passive and active, Hudec and Jackson 2007) (Figs. 3-5, 8 and 10a-b) along with small salt sheets by extrusion and thrusting (Figs. 4, 6 and 10b). A novel concept illustrated here is that coeval positioning of a salt structure over distinct base-salt domains results in complex, hybrid diapir growth characterized by alternating extensional and contractional regimes (Figs. 3-5, 10c-d). This occurs because the salt structure (i.e. diapir or anticline) is simultaneously influenced by contrasting flux variations and stress regimes on its flanks when these are located over distinct base-salt domains. Anticlines inflate over base-salt landward-dipping ramps whilst being asymmetrically extended and pierced by reactive diapirs over basinward-dipping ramps (anticline over fault-block B in fig. 4d-e and updip anticlines in figs. 3, 5 and 10d). Conversely, a diapir rises by extension over the footwall crest of basinward-dipping faults whilst actively piercing and upturning its roof above the base of the fault (hybrid diapir, fig. 4d and 10c). This phenomenon has been briefly described in an area of thick salt and prominent base-salt relief in the Santos Basin (Pichel et al., 2018), and also recognized over allochthonous salt in the Gulf of Mexico (Duffy, O., Peel, F. pers. comm. 2018).

In these settings, as salt and overburden translate downdip, salt flux variations and overburden deformation are driven primarily by shear-drag (i.e. Couette-flow) within the salt, a process illustrated in dynamic models based on our experiments (Fig. 9a-c). Earlier numerical simulations reproducing viscous salt drag and overburden translation (SaltDragON, Peel©) exhibit remarkably similar kinematics associated with simpler flat-ramp systems (Pichel et al., 2018). These models accurately simulate salt flux variations, sedimentation and development of asymmetric minibasins, i.e. ramp-syncline basins (Pichel et al., 2018), but do not reproduce lateral overburden deformation (i.e. extension and contraction) nor diapirism. The models presented here complement this earlier work by showing the effects of non-uniform translation over complex base-salt relief, resultant overburden contraction and extension patterns (i.e. folding, faulting) and diapirism. These are, nonetheless, simplifications of salt flow in nature, which is typically hybrid and simultaneously affected by varying proportions of Couette and Poiseuille flow components (Rowan et al., 2004; Weijermars et al., 2014; Pichel et al., 2018).

Variable pre-salt structural relief and sub-basin connectivity have a significant impact on flow kinematics and overburden deformation. Higher pre-salt fault topography and associated differences in salt thickness across neighbouring sub-basins produce stronger flux variations and disruptions. This produces greater updip inflation and contraction over landward-dipping base-salt ramps combined with greater downdip subsidence and associated extension and contraction over basinward-dipping base-salt ramps (Figs. 6-7). In cases where sub-basins are initially disconnected, they evolve independently until inflated salt from the updip graben is able to advance seaward over the downdip graben (Fig. 6d and 7d). In these cases, the final observed distribution of extensional and contractional strain is more localized and repeated on each half-graben (Figs. 6d and 7d). The width and magnitude of localized strain provinces is directly proportional to the width and steepness of the base-salt steps they are associated with (Figs. 4-8). Steep and narrow steps result in stronger, more abrupt salt flux changes and deformation over a narrower region, whereas gentle and wider ramps produce deformation that is more subtle but over a wider area (Figs. 4-8).

7.2. Applicability and Comparison with Seismic Examples

The models have limitations associated with free-edge effects and moving boundaries (c.f. Hardy and Finch, 2005; Pichel et al., 2017). Small-scale structures and the degree of faulting might differ locally from natural examples as these are affected by other variables not modelled here, e.g. changes in sedimentation pattern, loading, intra-salt stratigraphy, and tectonic reactivation. Nonetheless, our models produce salt flux variations, diapirism and distribution of structural styles similar to most recent physical experiments (Dooley et al., 2017) (compare fig. 1b and 8a), and examples of syn- and post-rift salt basins (Figs 11 and 12). The benefits of using DEM to model translation and salt flux variations over significantly variable base-salt topography are that results are easily reproducible and afford analysis of the sequential evolution of highly-strained systems and diapirs in cross-section. This is crucial to understand the distribution of salt and overburden geometries that undergo a complex, multiphase history of extension and contraction. Discrete-element models

(DEM) cannot substitute finite-element models (FEM) or physical models as these methods have other advantages; but the DEM technique applied here complements these other approaches improving the understanding of regional salt tectonics.

Results presented here are especially applicable to late syn-rift salt basins, which are mainly affected by thin-skinned salt tectonics and present wedge-shaped salt sequences across half-grabens (Rowan 2014; Jackson and Hudec, 2017). Examples of these basins include Nova Scotia (Fig. 11) (Albertz and Ings, 2010; Deptuck and Kendall; 2017), offshore Morocco, Mauritania (Davison 2005; Tari and Jabbour, 2013; Tari et al., 2017) and the Red Sea (Mitchell et al 2010; Rowan 2014). Additionally, initial basin geometries used in these models can also be applicable to segments of post-rift salt basins where significant base-salt topography is inherited from previous phases of rifting. Examples include Santos (Fig. 12) (Davison et al., 2012; Pichel et al., 2018); Campos (Davison et al., 2012; Dooley et al., 2017), Kwanza and Lower Congo (Hudec and Jackson 2004; Jackson and Hudec, 2005; Peel 2014); and Gulf of Mexico (Hudec et al., 2013; Dooley and Hudec, 2017).

As seen in examples of syn-rift salt, at the top of pre-salt faults and footwalls that define base-salt basinward-dipping ramps, deformation is characterized by extension (i.e. salt rollers and normal faults, Fig. 11). Conversely, at the base of basinward-dipping faults and/or over landward-dipping faults or footwalls, deformation is characterized by salt inflation and contraction, which are evidenced by fault inversion and thrusting (Fig. 11a), and diapir squeezing (Fig. 11b).

In the case of post-rift salt in the Santos Basin, variations of base-salt relief are less pronounced but the strain and structural style distribution are remarkably similar (Fig. 12). Salt anticlines form by contraction (indicated by intra-salt seaward-vergent shear zones) above base-salt landward-dipping ramps, being asymmetrically extended later by basinward-dipping normal faults above a broadly flat base-salt high (Fig. 12a-b). Deformation over most of this horst is dominated by extension and widening of earlier salt anticlines, and reactive diapirs characterized by a triangular shape and inward-dipping and younging growth normal faults (Fig. 12a-c). Minor later inflation occurred as structures approached a subtle landward-dipping base-salt step near the horst margin, so the earlier reactive diapir uplifted a post-extension broadly tabular roof (Fig. 12c).

Further downdip, deformation is characterized by a monoclinal zone of subsidence over a large basinward-dipping base-salt ramp defined by a set of basinward-dipping normal faults (Fig. 12a). This zone of subsidence is characterized by updip extension and downdip contraction as in the models presented here (Fig. 9 and 12). An earlier salt anticline is extended at the crest of this ramp (Fig 12d), while a fold-thrust belt develops at and downdip of the base of the ramp (Fig. 12e).

Models simulating variable base-salt step height (Figs. 7-8) can help clarify along-strike variations of salt-related structural styles in rifted passive margins due to variable pre-salt rift geometries, fault throw, spacing and polarity (Fig. 13). An increase of throw along-strike for basinward-dipping faults results in greater inflation over the footwalls and subsidence above the faults with, consequently, greater extension at the footwall crest and contraction at the base of the fault (Fig. 13a). Thus, greater base-salt relief, usually near the centre of syn-rift faults, can produce increased salt rise and diapirism (Fig. 13a), whereas towards the fault tips, structures tend to be more subtle and dominated by salt subsidence and inflated anticlines (Fig. 13b). Closely-spaced fault-blocks generate more abrupt flux variations and buttressing at the base of the ramp and against the footwall, amplifying contraction and squeezing of earlier structures (left-hand side, Fig. 13a). Buttressing and contraction are also increased in the case of a reversal in fault polarity (i.e. landward-dipping faults) producing larger salt anticlines and less diapirism (Fig. 13c).

8. Conclusions

The results reproduce expected salt flux variations, diapirism and structural styles according to previous physical experiments simulating similar, albeit simpler, scenarios; exhibiting additional detail in the cross-sectional, multiphase evolution of these systems. Models illustrate how pre-salt relief nucleates salt and supra-salt structures by producing changes in salt flow and stress patterns in the overburden during early-stage gliding in passive margins. More complex and realistic pre-salt rift geometries are simulated (i.e. tilted fault-blocks), demonstrating how sets of variably-dipping base-salt ramps complicate salt flow and overburden deformation by promoting more abrupt flux variations and multiphase evolution of salt structures. Multiple and connected base-salt ramps having variable slopes related to tilted fault-blocks produce higher-frequency variation of structural styles, strain distribution and overlap than in simpler flat-ramp base-salt systems defined by pre-salt horsts. Results also demonstrate how variable height, dip and orientation of pre-salt structures play a key role on the evolution of these systems and can partially explain along-strike variation of salt-related deformation in rifted margins.

Salt and supra-salt gliding over tilted-blocks defined by basinward-dipping faults results in wide, low amplitude zones of inflation above footwalls and abrupt subsidence over steep fault-scarps with reactive diapirs that are squeezed and extrude salt sheets as they move across pre-salt faults. Translation over tilted-blocks defined by landward-dipping faults produces narrow zones of inflation over the steep fault-scarp and overall greater contraction and less diapirism as flow is buttressed by base-salt steps dipping contrary to flow direction. As salt and cover move downdip, structures translate over contrasting structural domains, being inverted and/or growing asymmetrically.

Models reproduce similar geometries and distribution of structural styles to seismic examples of both syn- and post-rift salt basins where prominent base-salt topography exists. They also demonstrate an important component of multiphase, asymmetric diapir growth and cover deformation that is observed in modern, high-resolution 3D-seismic data and relates to differential salt flow and flux variations over pre-salt relief. These results work as a guide to the interpretation of complex diapir geometries, their multiphase growth history and structural style variation in salt basins; ultimately increasing the understanding of this novel and important aspect of salt tectonics.

Acknowledgments

We wish to thank Christopher Jackson, Frank Peel, Jonathan Redfern, Tim Dooley and Oliver Duffy for sharing their insights and for fruitful discussions. We thank CGG for providing access to 3D seismic dataset and the section presented from the Santos Basin. The first author would like to thank the Science without Borders program and CNPq, Brazil for sponsoring his PhD research. The North Africa Research Group (University of Manchester) and its sponsors are also acknowledged for providing substantial support during the main author's PhD. We also thank the Norwegian Academy of Science and Letters VISTA program for funding the first author's visiting position at the University of Bergen where most of this research was conducted and Gawthorpe's VISTA Professorship. The modelling data can be

obtained from link: https://www.researchgate.net/publication/329844061_Discrete-Element_Modeling_data_of_salt-related_translation_over_pre-salt_rift_structures.

Figures and Table Captions

Table 1: Summary of variable input parameters for all models.

Figure 1: (a) Classical distribution of regional salt tectonics structural domains in passive margins: updip extensional and downdip contractional domains kinematically linked by an undeformed translational province (from Jackson et al., 2015). (b) Kinematic model based on recent physical experiments showing two-stages effects of salt-related translation across basement topography and consequent variations of salt flux resulting in complex, multiphase deformation history (from Dooley et al., 2017).

Figure 2: Initial experiment designs, dimensions and thicknesses after a phase of particle settling for the main experiments presented in this study: (a) Model A: horst block; (b) Model B: basinward-dipping normal faults; (c) Model C: landward-dipping normal faults; (d) focused views showing variation of structural relief and salt connectivity for basinward-dipping normal faults (Models B1-B4); and (e) for landward-dipping normal faults (Models C1-C4). The modelled media consists of a box with free walls and rigid, undeformable pre-salt structures (black). The models have an initial thickness of 3 km, with the salt section (magenta) having a maximum thickness of 2.1 km and minimum thickness over the footwall crest decreasing as the structural relief increases for models B1-B4 and C1-C4, with no salt over the footwall crest of models B4 and C4. The pre-kinematic overburden (green) has constant thickness of 900 m.

Figure 3: Sequential evolution shown in increments of 2 Ma (a-e) of Model A: Horst Block, which simulates translation over a single pre-salt horst and consequent salt flux variations across a simple base-salt topography. Model edges are not shown to improve visualization of relevant structures at the centre of the model. As the system translates, structures move over different structural domains, being reactivated and/or inverted. These extensional (black box) and contractional (white boxes) domains shift over time. Diapirs are represented by numbers 1-7 and their corresponding style of growth is indicated in subscript.

Figure 4: Sequential evolution shown in increments of 2 Ma (a-e) of Model B: Basinward-dipping Normal Faults, simulating translation over tilted fault-blocks (A and B). Each of these blocks defines a gentle landward-dipping base-salt ramp and a steep basinward-dipping base-salt ramp. To improve visualization of relevant structures only the centre of the model is shown. Salt flux variations occur above each ramp segment complicating flow kinematics and overburden deformation. As the system translates, structures move over different structural domains, being reactivated and/or inverted. Extensional (black boxes) and contractional (white boxes) domains occur over each fault-block, which change through time. Diapirs are represented by numbers 1-6 and their corresponding style of growth in subscript. A salt sheet (S_1) forms due to diapir squeezing at the bottom of the distal basinward-dipping ramp.

Figure 5: Sequential evolution presented in increments of 2 Ma (a-e) of Model C: Landward-dipping Normal Faults, which simulates salt-detached translation over a pair of tilted fault-blocks defining steep landward-dipping base-salt ramps updip and gentle basinward-dipping base-salt ramps downdip. To improve visualization of relevant structures at the centre of the model, its edges are not shown. Contractional (lower white boxes) domains and extensional

(lower black boxes) occur over each half-graben by the end of the experiment. Diapirs are represented by numbers 1-3 and their corresponding style of growth in subscripted letters.

Figure 6: Final results (after 10 Myr) showing the effects of salt connectivity and pre-salt step height on lateral salt flow, diapirism and overburden deformation for tilted fault-blocks defined by basinward-dipping faults: (a) B1, (b) B2, (c) B3, and (d) B4. Maximum salt thickness in all models is 2.1 km at the deepest portion of the graben and minimum salt thickness is of 900 m (B1), 600 m (B2), 300 m (B3) and 0 m (B4) over the pre-salt structural highs. Model boundaries are far from the section of the model shown so structures are not affected by boundary artefacts. Zones of updip inflation are shown by white horizontal lines and zones of extension by black horizontal. Norma faults are in black and reverse faults in orange.

Figure 7: Final (after 10 Myr) results showing the effects of salt connectivity and pre-salt step height on lateral salt flow, diapirism and overburden deformation for tilted fault-blocks defined by landward-dipping faults: (a) C1, (b) C2, (c) C3, and (d) C4. Maximum salt thickness in all models is 2.1 km at the deepest portion of the graben and minimum salt thickness is of 900 m (B1), 600 m (B2), 300 m (B3) and 0 m (B4) over the pre-salt structural highs. White dashed-lines represent original top salt (T_0). Model boundaries are far from the section of the model shown so structures are not affected by boundary artefacts. Zones of inflation are indicated by white dashed lines. Norma faults are in black and reverse faults in orange.

Figure 8: Synthesis diagram of final model results comparing structural style distribution associated with (a) a pre-salt horst, and pairs of tilted fault-blocks defined by (b) basinward-dipping and (c) landward-dipping pre-salt rift faults. (S) indicates zones of subsidence and (I) zones of inflation and contraction. The distribution of structural domains is shown at the bottom of each section with extensional domains in black boxes and contractional domains in white boxes. Normal faults are shown in black and reverse faults in red. Pre-salt rift structures are in black, salt in pink and overburden in light green.

Figure 9: Simplified diagram based on model results illustrating initial salt structures and the dynamics of viscous shear (Couette salt flow) and flow perturbations related to gliding and salt flux changes due to variations in original salt thickness across pre-salt topography: (a) pre-salt horst; and pairs of tilted fault-blocks defined by (b) basinward-dipping and (c) landward-dipping pre-salt rift faults.

Figure 10: Focused sections showing examples of salt response and complex, multiphase styles of diapirism associated with flow over base-salt ramps. (a) After continuous extension, a reactive (i.e. extensional) diapir reaches the surface and continues to evolve as a passive diapir (1_P) at an extensional hinge at the crest of a basinward-dipping normal fault of Model B (4 Myr). (b) Reactive diapirs are squeezed (1_S, 2_S and 3_S) and normal faults inverted as they move over the base of the basinward-dipping (BW) fault (contractional hinge) with salt sheet extruding from the crest of the basinwardmost diapir (1_S) in Model B (10 Myr). (c) Hybrid diapir characterized by extension and reactive rise over the footwall crest (extensional hinge) and active diapirism and flank upturn over the base of the fault (contractional hinge) in Model B (8 Myr). (d) Salt anticline inflates over a landward-dipping fault whilst its downdip flank collapses, being extended and pierced by reactive diapirs over the basinward-dipping dip-slope in Model C (10 Myr).

Figure 11: Seismic examples of the impact of complex pre-salt syn-rift topography on salt tectonics of a late syn-rift salt basin in Nova Scotia (modified from Deptuck and Kendell, 2017). (a) Movement over a pair of steep basinward- (BW) and landward (LW)-dipping ramps produces extension at the top of the basinward-dipping ramp and simultaneous

contraction and uplift at its bottom and over the landward-dipping ramp. Further downdip, another zone of extension and salt expulsion occurs at the top of a gentle basinward-dipping step while a previous extensional minibasin is translated basinward, being contracted at the bottom of this ramp and over a small landward-dipping step. (b) Extension occurs at the top of a gentle basinward-dipping ramp; while a previously reactive/passive diapir formed further updip is squeezed as it is buttressed against a steep landward-dipping pre-salt step.

Figure 12: (a) High-resolution regional seismic section illustrating the effects of complex pre-salt relief on salt flow in a post-rift salt basin, Santos Basin, Brazil. Salt is on average 2 km thick and has a prominent intra-salt layering, which works as kinematic indicator. (b)-(e) Close-ups. (b) Movement over a landward-dipping base-salt step results in contraction (evidenced by basinward-vergent intra-salt shear zone) and development of a salt anticline that is asymmetrically extended above the base-salt high. Over the pre-salt horst, deformation is driven mainly by extension and reactive diapirism. (c) Close-up of reactive diapir shows growth strata associated to normal faults and later uplift of a tabular roof with growth strata in yellow. At the downdip edge of the tilted fault-block, movement over the pre-salt footwall crest (FW crest) and basinward-dipping fault produces a zone of extension at the top (d) and contraction (fold-thrust-belt) at its base (e).

Figure 13: Along-strike variation of salt structural domains associated with pre-salt rift topography, fault polarity and throw variations (. Profile (a) shows variations related to high-relief as well as closely-spaced basinward-dipping rift faults, whereas profile (b) illustrates variations associated with low-relief basinward-dipping faults and profile (c) landward-dipping faults.

References

Abe, S., & Urai, J. L. (2012). Discrete element modeling of boudinage: Insights on rock rheology, matrix flow, and evolution of geometry. Journal of Geophysical Research: Solid Earth, 117(B1). https://doi.org/10.1029/2011JB008555

Adam, J., & Krézsek, C. (2012). Basin-scale salt tectonic processes of the Laurentian Basin, Eastern Canada: insights from integrated regional 2D seismic interpretation and 4D physical experiments. Geological Society, London, Special Publications, 363, 331-360. https://doi.org/10.1144/SP363.15

Albertz, M., Beaumont, C., Shimeld, J. W., Ings, S. J., & Gradmann, S. (2010). An investigation of salt tectonic structural styles in the Scotian Basin, offshore Atlantic Canada: 1. Comparison of observations with geometrically simple numerical models. Tectonics, 29(4). https://doi.org/10.1029/2009TC002539

Allen, M. P., Tildesley, D. J. (1987). Molecular Simulation of Liquids. Clarendon, Oxford.

Botter, C., Cardozo, N., Hardy, S., Lecomte, I., & Escalona, A. (2014). From mechanical modeling to seismic imaging of faults: A synthetic workflow to study the impact of faults on seismic. Marine and Petroleum Geology, 57, 187-207. https://doi.org/10.1016/j.marpetgeo.2014.05.013

Brun, J. P., & Fort, X. (2011). Salt tectonics at passive margins: Geology versus models. Marine and Petroleum Geology, 28(6), 1123-1145. https://doi.org/10.1016/j.marpetgeo.2011.03.004

Davison, I., (2005). Central Atlantic margin basins of North West Africa: geology and hydrocarbon potential (Morocco to Guinea). Journal of African Earth Sciences, 43(1), 254-274. https://doi.org/10.1016/j.jafrearsci.2005.07.018

Davison, I., Anderson, L., & Nuttall, P., (2012). Salt deposition, loading and gravity drainage in the Campos and Santos salt basins. Geological Society, London, Special Publications, 363, 159-174. https://doi.org/10.1144/SP363.8

Deng, C., Gawthorpe, R. L., Finch, E., & Fossen, H. (2017). Influence of a pre-existing basement weakness on normal fault growth during oblique extension: Insights from discrete element modeling. Journal of Structural Geology, 105, 44-61. https://doi.org/10.1016/j.jsg.2017.11.005

Deptuck, M. E., & Kendell, K. L. (2017). A review of Mesozoic-Cenozoic Salt Tectonics Along the Scotian Margin, Eastern Canada. In: Soto, J. I., Flinch, J., & Tari, G. (Eds.). (2017). Permo-Triassic Salt Provinces of Europe, North Africa and the Atlantic Margins: Tectonics and Hydrocarbon Potential. Elsevier, 287-312. https://doi.org/10.1016/B978-0-12-809417-4.00014-8

Donzé, F., Mora, P., & Magnier, S. A., (1994). Numerical simulation of faults and shear zones. Geophysical Journal International, 116(1), 46-52. https://doi.org/10.1111/j.1365-246X.1994.tb02126.x

Dooley, T. P., Jackson, M., & Hudec, M. R., (2007). Initiation and growth of salt-based thrust belts on passive margins: results from physical models. Basin Research, 19(1), 165-177. https://doi.org/10.1111/j.1365-2117.2007.00317.x

Dooley, T. P., Jackson, M. P., & Hudec, M. R., (2009). Inflation and deflation of deeply buried salt stocks during lateral shortening. Journal of Structural Geology, 31(6), 582-600. https://doi.org/10.1016/j.jsg.2009.03.013

Dooley, T. P., Hudec, M. R., & Jackson, M. P., (2012). The structure and evolution of sutures in allochthonous salt. AAPG bulletin, 96(6), 1045-1070. https://doi.org/10.1306/09231111036

Dooley, T. P., Jackson, M. P. A., & Hudec, M. R., (2015). Breakout of squeezed stocks: dispersal of roof fragments, source of extrusive salt and interaction with regional thrust faults. Basin Research, 27(1), 3-25. https://doi.org/10.1111/bre.12056

Dooley, T. P., Hudec, M. R., Carruthers, D., Jackson, M. P., & Luo, G., (2017). The effects of base-salt relief on salt flow and suprasalt deformation patterns—Part 1: Flow across simple steps in the base of salt. Interpretation, 5(1), SD1-SD23. https://doi.org/10.1190/INT-2016-0087.1

Dooley, T. P., & Hudec, M. R. (2017). The effects of base-salt relief on salt flow and suprasalt deformation patterns—Part 2: Application to the eastern Gulf of Mexico. Interpretation, 5(1), SD25-SD38. https://doi.org/10.1190/INT-2016-0088.1

Duffy, O. B., Gawthorpe, R. L., Docherty, M., & Brocklehurst, S. H. (2013). Mobile evaporite controls on the structural style and evolution of rift basins: Danish Central Graben, North Sea. Basin Research, 25(3), 310-330. https://doi.org/10.1111/bre.12000

Ferrer, O., Jackson, M. P. A., Roca, E., & Rubinat, M., (2012). Evolution of salt structures during extension and inversion of the Offshore Parentis Basin (Eastern Bay of Biscay). Geological Society, London, Special Publications, 363, 361-380. https://doi.org/10.1144/SP363.16

Ferrer, O., McClay, K., & Sellier, N. C., (2017). Influence of fault geometries and mechanical anisotropies on the growth and inversion of hanging-wall synclinal basins: insights from sandbox models and natural examples. Geological Society, London, Special Publications, 439, 487-509. https://doi.org/10.1144/SP439.8

Finch, E., Hardy, S., & Gawthorpe, R., (2003). Discrete element modelling of contractional fault-propagation folding above rigid basement fault blocks. Journal of Structural Geology, 25(4), 515-528. https://doi.org/10.1016/S0191-8141(02)00053-6

Finch, E., Hardy, S., & Gawthorpe, R., (2004). Discrete-element modelling of extensional fault-propagation folding above rigid basement fault blocks. Basin Research, 16(4), 467-488. https://doi.org/10.1111/j.1365-2117.2004.00241.x

Finch, E., & Gawthorpe, R., (2017). Growth and interaction of normal faults and fault network evolution in rifts: insights from three-dimensional discrete element modelling. Geological Society, London, Special Publications, 439, SP439-23. https://doi.org/10.1144/SP439.23

Gawthorpe, R. L., & Leeder, M. R. (2000). Tectono-sedimentary evolution of active extensional basins. Basin Research, 12(3-4), 195-218. https://doi.org/10.1111/j.1365-2117.2000.00121.x

Ge, H., Jackson, M. P., & Vendeville, B. C., (1997). Kinematics and dynamics of salt tectonics driven by progradation. AAPG Bulletin, 81(3), 398-423.

Gemmer, L., Ings, S. J., Medvedev, S., & Beaumont, C., (2004). Salt tectonics driven by differential sediment loading: stability analysis and finite-element experiments. Basin Research, 16(2), 199-218. https://doi.org/10.1111/j.1365-2117.2004.00229.x

Gemmer, L., Beaumont, C., & Ings, S. J., (2005). Dynamic modelling of passive margin salt tectonics: effects of water loading, sediment properties and sedimentation patterns. Basin Research, 17(3), 383-402. https://doi.org/10.1111/j.1365-2117.2005.00274.x

Gradmann, S., Beaumont, C., & Albertz, M., (2009). Factors controlling the evolution of the Perdido Fold Belt, northwestern Gulf of Mexico, determined from numerical models. Tectonics, 28(2). https://doi.org/10.1029/2008TC002326

Gradmann, S., & Beaumont, C., (2016). Numerical modelling study of mechanisms of mid-basin salt canopy evolution and their potential applications to the Northwestern Gulf of Mexico. Basin Research 29(4), 490-520. https://doi.org/10.1111/bre.12186

Hardy, S., & Finch, E., (2005). Discrete-element modelling of detachment folding. Basin Research, 17(4), 507-520. https://doi.org/10.1111/j.1365-2117.2005.00280.x

Hardy, S., Finch, E., (2006). Discrete element modelling of the influence of cover strength on basement-involved fault-propagation folding. Tectonophysics, 415, 225-238. https://doi.org/10.1016/j.tecto.2006.01.002

Hardy, S., & Finch, E., (2007). Mechanical stratigraphy and the transition from trishear to kink-band fault-propagation fold forms above blind basement thrust faults: a discrete-element study. Marine and Petroleum Geology, 24(2), 75-90. https://doi.org/10.1016/j.marpetgeo.2006.09.001

Hudec, M. R., & Jackson, M. P., (2004). Regional restoration across the Kwanza Basin, Angola: Salt tectonics triggered by repeated uplift of a metastable passive margin. AAPG Bulletin, 88(7), 971-990. https://doi.org/10.1306/02050403061

Hudec, M. R., & Jackson, M. P., (2007). Terra infirma: Understanding salt tectonics. Earth-Science Reviews, 82(1), 1-28. https://doi.org/10.1016/j.earscirev.2007.01.001

Hudec, M. R., Norton, I. O., Jackson, M. P., & Peel, F. J., (2013). Jurassic evolution of the Gulf of Mexico salt basin. AAPG Bulletin, 97(10), 1683-1710. https://doi.org/10.1306/04011312073

Ings, S. J., & Shimeld, J. W. (2006). A new conceptual model for the structural evolution of a regional salt detachment on the northeast Scotian margin, offshore eastern Canada. AAPG Bulletin, 90(9), 1407-1423. https://doi.org/10.1306/04050605159

Jackson, C. A. L., Jackson, M. P., & Hudec, M. R., (2015). Understanding the kinematics of salt-bearing passive margins: A critical test of competing hypotheses for the origin of the Albian Gap, Santos Basin, offshore Brazil. Geological Society of America Bulletin, 127(11-12), 1730-1751. https://doi.org/10.1130/B31290.1

Jackson, C. A. L., Jackson, M. P., Hudec, M. R., & Rodriguez, C. R., (2015). Enigmatic structures within salt walls of the Santos Basin—Part 1: Geometry and kinematics from 3D seismic reflection and well data. Journal of Structural Geology, 75, 135-162. https://doi.org/10.1016/j.jsg.2015.01.010

Jackson, M. P., Hudec, M. R., Jennette, D. C., & Kilby, R. E., (2008). Evolution of the Cretaceous Astrid thrust belt in the ultradeep-water Lower Congo Basin, Gabon. AAPG Bulletin, 92(4), 487-511. https://doi.org/10.1306/12030707074

Jackson, M. P., & Hudec, M. R., (2017). Salt Tectonics: Principles and Practice. Cambridge University Press. https://doi.org/10.1017/9781139003988

Johnson, R. B., & DeGraff, J. V., (1988). Principles of engineering geology. Wiley.

Li, S. Y., & Urai, J. L., (2016). Rheology of rock salt for salt tectonics modeling. Petroleum Science, 13(4), 712-724.

Liang, W. G., Yang, C. H., Zhao, Y. S., Dusseault, M. B., & Liu, J., (2007). Experimental investigation of mechanical properties of bedded salt rock. International Journal of Rock Mechanics and Mining Sciences, 44(3), 400-411. https://doi.org/10.1016/j.ijrmms.2006.09.007

Mitchell, N. C., Ligi, M., Ferrante, V., Bonatti, E., & Rutter, E., (2010). Submarine salt flows in the central Red Sea. GSA Bulletin, 122(5-6), 701-713. https://doi.org/10.1130/B26518.1Mohriak, W.U., Macedo, J.M., Castellani, R.T., Rangel, H.D., Barros, A.Z.N., Latgé, M.A.L., Mizusaki, A.M.P., Szatmari, P., Demercian, L.S., Rizzo, J.G., & Aires, J.R., (1995). Salt tectonics and structural styles in the deep-water province of the Cabo Frio region, Rio de Janeiro, Brazil. in M. P. A. Jackson, D. G. Roberts, and S. Snelson, eds., Salt tectonics: a global perspective: AAPG Memoir 65, 273-304.

Mora, P., & Place, D., (1993). A lattice solid model for the nonlinear dynamics of earthquakes. International Journal of Modern Physics C, 4(06), 1059-1074. https://doi.org/10.1306/M65604C13

Mora, P., & Place, D., (1994). Simulation of the frictional stick-slip instability. Pure and applied geophysics, 143(1-3), 61-87. https://doi.org/10.1007/BF00874324

Peel, F. J. (2014). The engines of gravity-driven movement on passive margins: Quantifying the relative contribution of spreading vs. gravity sliding mechanisms. *Tectonophysics*, *633*, 126-142. https://doi.org/10.1016/j.tecto.2014.06.023

Pichel, L. M., Finch, E., Huuse, M., & Redfern, J., (2017). The influence of shortening and sedimentation on rejuvenation of salt diapirs: A new Discrete-Element Modelling approach. Journal of Structural Geology, 104, 61-79.

Pichel, L.M., Peel, F., Jackson, C.A.-L., Huuse, M., 2018, Geometry and kinematics of salt-detached ramp syncline basins, Journal of Structural Geology, 115, 208-230. , doi: 10.1016/ j.jsg.2018.07.016.

Place, D., Lombard, F., Mora, P., & Abe, S., (2002). Simulation of the micro-physics of rocks using LSMearth. In Earthquake Processes: Physical Modelling, Numerical

Simulation and Data Analysis Part I (pp. 1911-1932). Birkhäuser Basel. https://doi.org/10.1007/s00024-002-8715-x

Quirk, D. G., Schødt, N., Lassen, B., Ings, S. J., Hsu, D., Hirsch, K. K., & Von Nicolai, C., (2012). Salt tectonics on passive margins: examples from Santos, Campos and Kwanza basins. Geological Society, London, Special Publications, 363, 207-244. https://doi.org/10.1144/SP363.10Rowan, M. G., (1995). Structural styles and evolution of allochthonous salt, central Louisiana outer shelf and upper slope, in M. P. A. Jackson, D. G. Roberts, and S. Snelson, eds., Salt tectonics: a global perspective: AAPG Memoir 65, 199-228. https://doi.org/10.1306/M65604C9

Rowan, M. G., Trudgill, B. D., & Carl Fiduk, J., (2000). Deep-Water, Salt-Cored Foldbelts: Lessons from the Mississippi Fan and Perdido Foldbelts, Northern Gulf of Mexico. Atlantic rifts and continental margins, 173-191. *Geophysical Monograph-American Geophysical Union*, *115*, 173-192. https://doi.org/10.1029/GM115p0173

Rowan, M. G., Peel, F. J., & Vendeville, B. C., (2004). Gravity-driven fold belts on passive margins. In: McKlay, K.R. (Ed.) Thrust tectonics and Hydrocarbon Systems. AAPG Memoir 82, 157-182. https://doi.org/10.1306/M82813C9

Rowan, M. G. (2014). Passive-margin salt basins: hyperextension, evaporite deposition, and salt tectonics. Basin Research, 26(1), 154-182. https://doi.org/10.1111/bre.12043

Schöpfer, M. P. J., Childs, C. & Walsh, J. J., (2006). Localisation of normal faults in multilayer sequences. Journal of Structural Geology, 28, 816-833. https://doi.org/10.1016/j.jsg.2006.02.003

Schultz-Ela, D. D., Jackson, M. P., & Vendeville, B. C., (1993). Mechanics of active salt diapirism. Tectonophysics, 228(3-4), 275-312. https://doi.org/10.1016/0040-1951(93)90345-K

Spiers, C. J., Schutjens, P. M. T. M., Brzesowsky, R. H., Peach, C. J., Liezenberg, J. L., & Zwart, H. J., (1990). Experimental determination of constitutive parameters governing creep of rocksalt by pressure solution. Geological Society, London, Special Publications, 54, 215-227. https://doi.org/10.1144/GSL.SP.1990.054.01.21

Tari, G., Molnar, J., Ashton, P., & Hedley, R., (2000). Salt tectonics in the Atlantic margin of Morocco. The Leading Edge, 19(10), 1074-1078. https://doi.org/10.1190/1.1438481

Tari, G., Molnar, J., & Ashton, P., (2003). Examples of salt tectonics from West Africa: a comparative approach. Geological Society, London, Special Publications, 207, 85-104. https://doi.org/10.1144/GSL.SP.2003.207.5

Tari, G., & Jabour, H., (2013). Salt tectonics along the Atlantic margin of Morocco. Geological Society, London, Special Publications, 369, 337-353. https://doi.org/10.1144/SP369.23

Tari, G., Novotny, B., Jabour, H., & Hafid, M., (2017). Salt tectonics along the Atlantic Margin of NW Africa (Morocco and Mauritania). In: Soto, J. I., Flinch, J., & Tari, G. (Eds.). (2017). Permo-Triassic Salt Provinces of Europe, North Africa and the Atlantic Margins: Tectonics and Hydrocarbon Potential. Elsevier, 331-351. https://doi.org/10.1016/B978-0-12-809417-4.00016-1

Vendeville, B. C., & Jackson, M. P. A., (1992). The rise of diapirs during thin-skinned extension. Marine and Petroleum Geology, 9(4), 331-354. https://doi.org/10.1016/0264-8172(92)90047-I

Vendeville, B. C., Ge, H., & Jackson, M. P. A., (1995). Scale models of salt tectonics during basement-involved extension. Petroleum Geoscience, 1(2), 179-183. https://doi.org/10.1144/petgeo.1.2.179

Wagner, B. H., & Jackson, M. P., (2011). Viscous flow during salt welding. Tectonophysics, 510(3), 309-326. https://doi.org/10.1016/j.tecto.2011.07.012

Weijermars, R., & Schmeling, H., (1986). Scaling of Newtonian and non-Newtonian fluid dynamics without inertia for quantitative modelling of rock flow due to gravity (including the concept of rheological similarity). Physics of the Earth and Planetary Interiors, 43(4), 316-330. https://doi.org/10.1016/0031-9201(86)90021-X

Weijermars, R., Jackson, M. T., & Vendeville, B., (1993). Rheological and tectonic modeling of salt provinces. Tectonophysics, 217(1-2), 143-174. https://doi.org/10.1016/0040-1951(93)90208-2

Weijermars, R., Hudec, M. R., Dooley, T. P., & Jackson, M. P. A., (2015). Downbuilding salt stocks and sheets quantified in 3-D analytical models. Journal of Geophysical Research: Solid Earth, 120(6), 4616-4644. https://doi.org/10.1002/2014JB011704

Figures and Tables

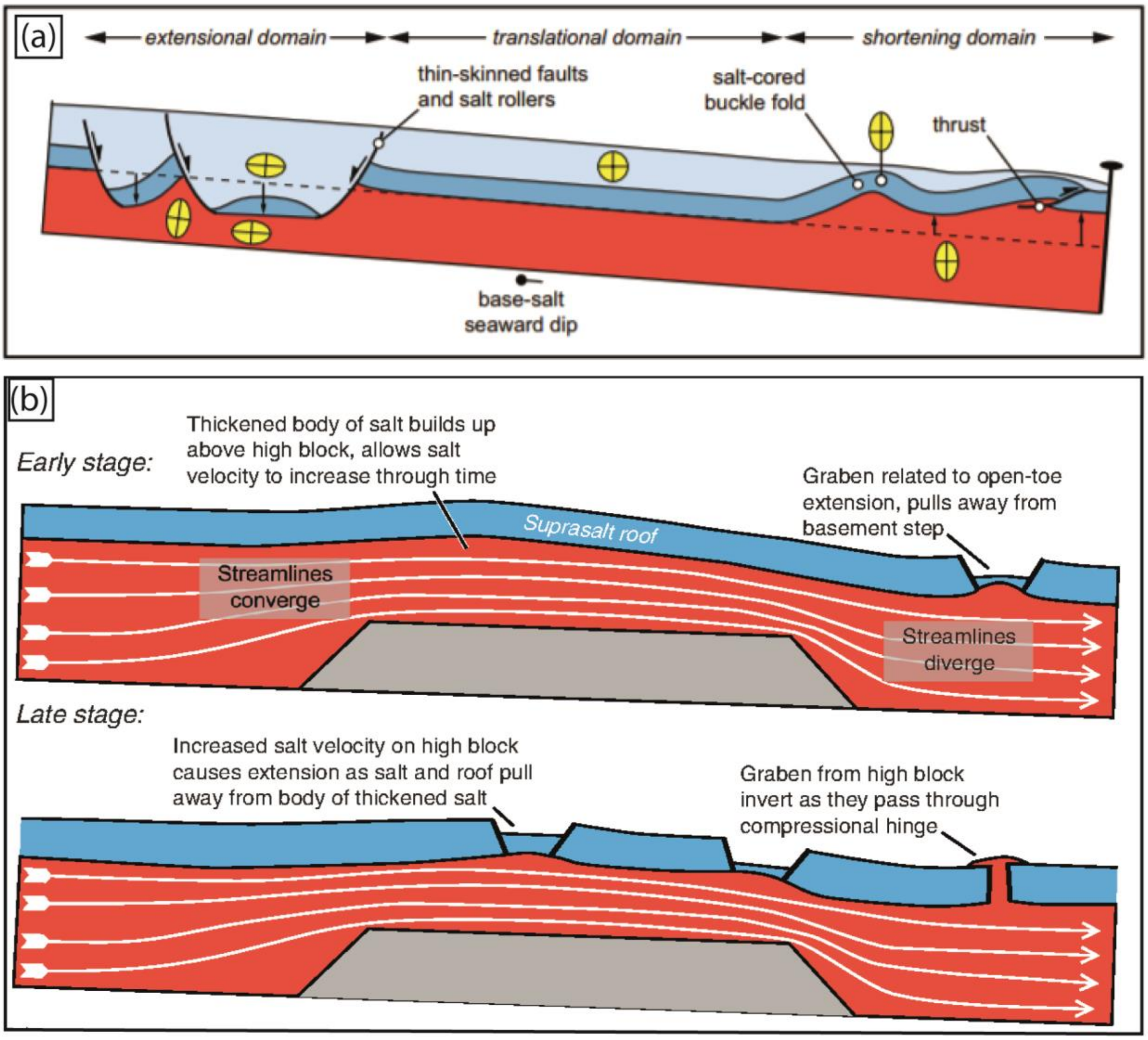

Figure 1

1047

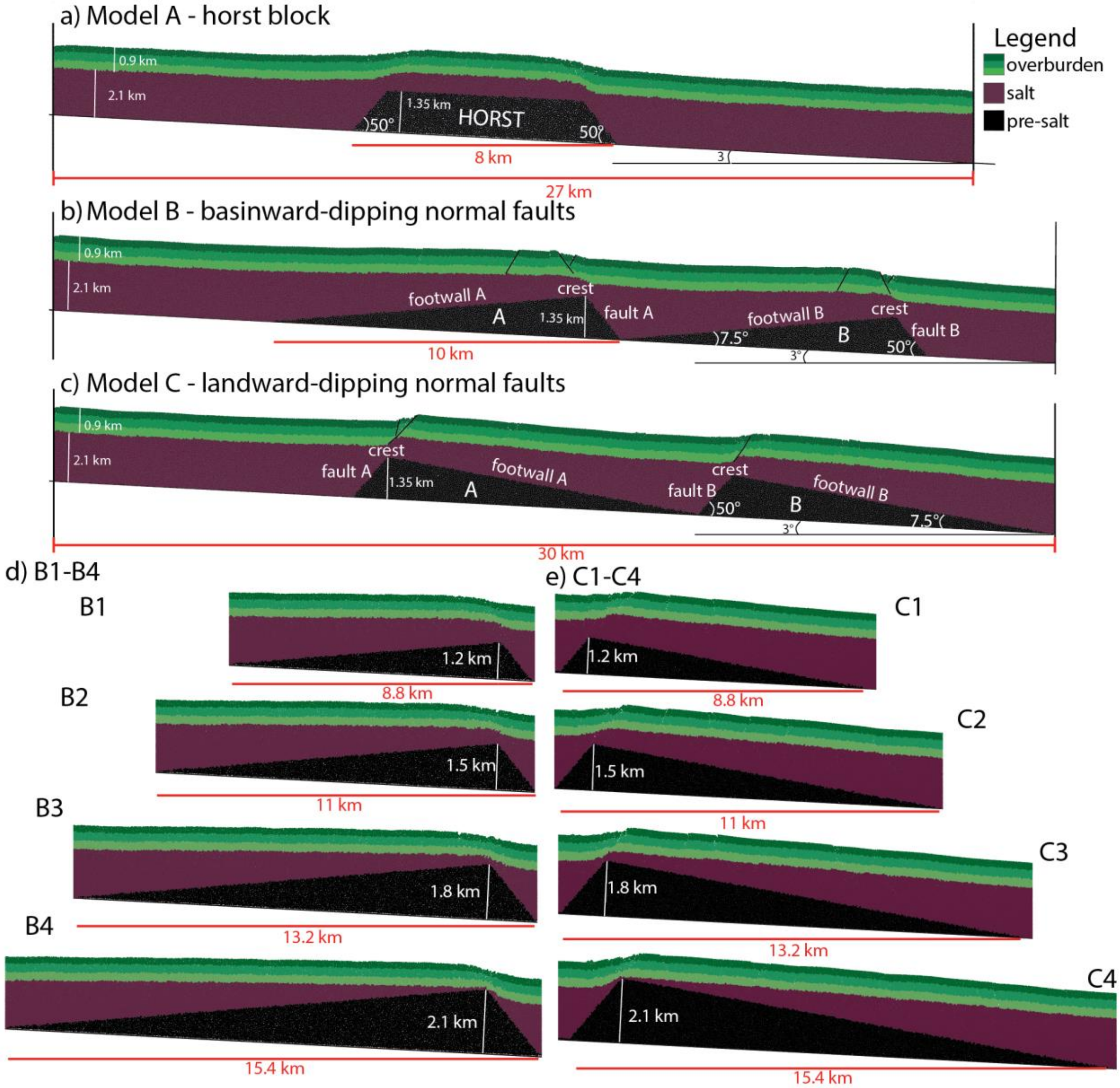

1048 Figure 2

1049

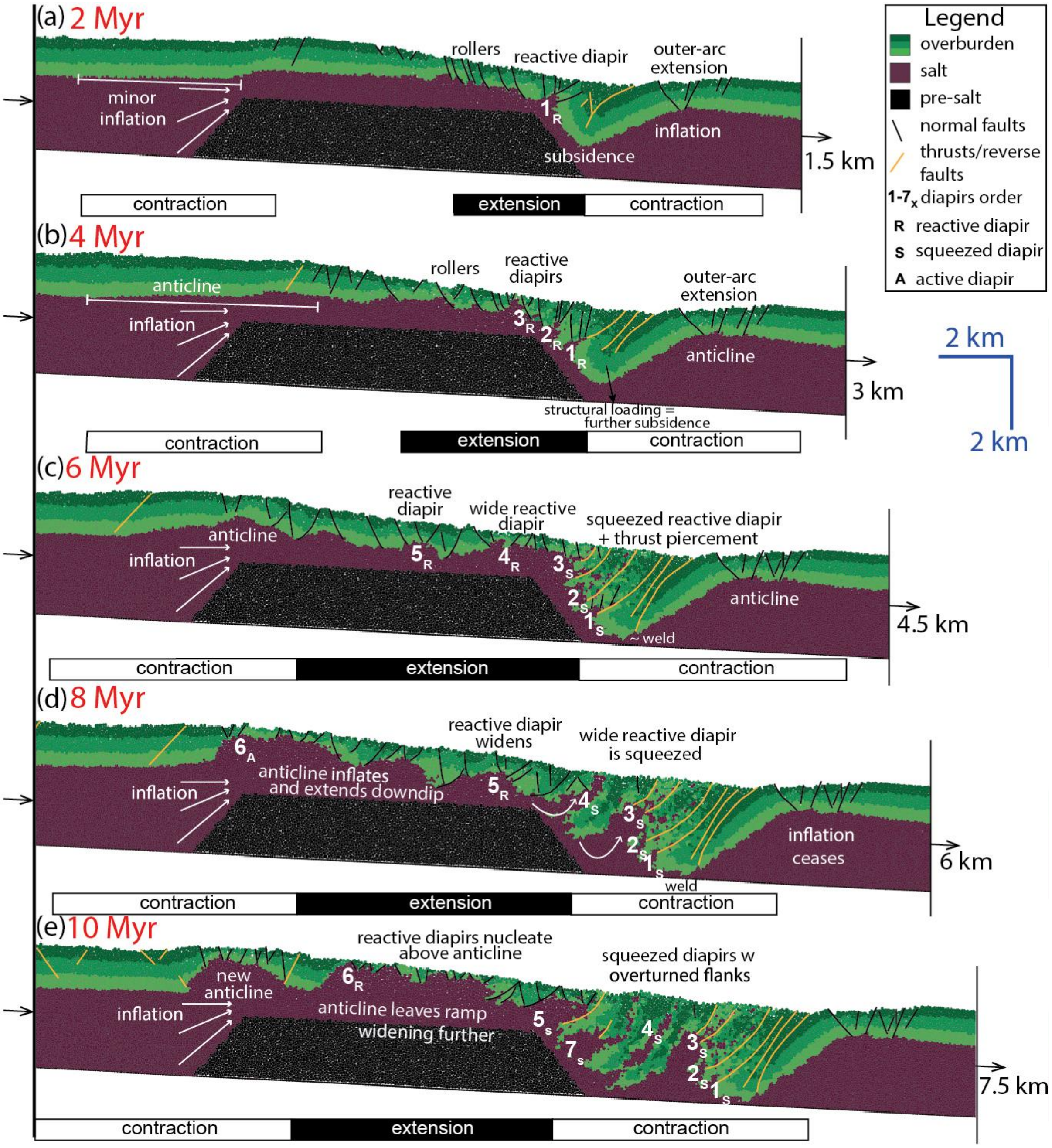

1050 Figure 3

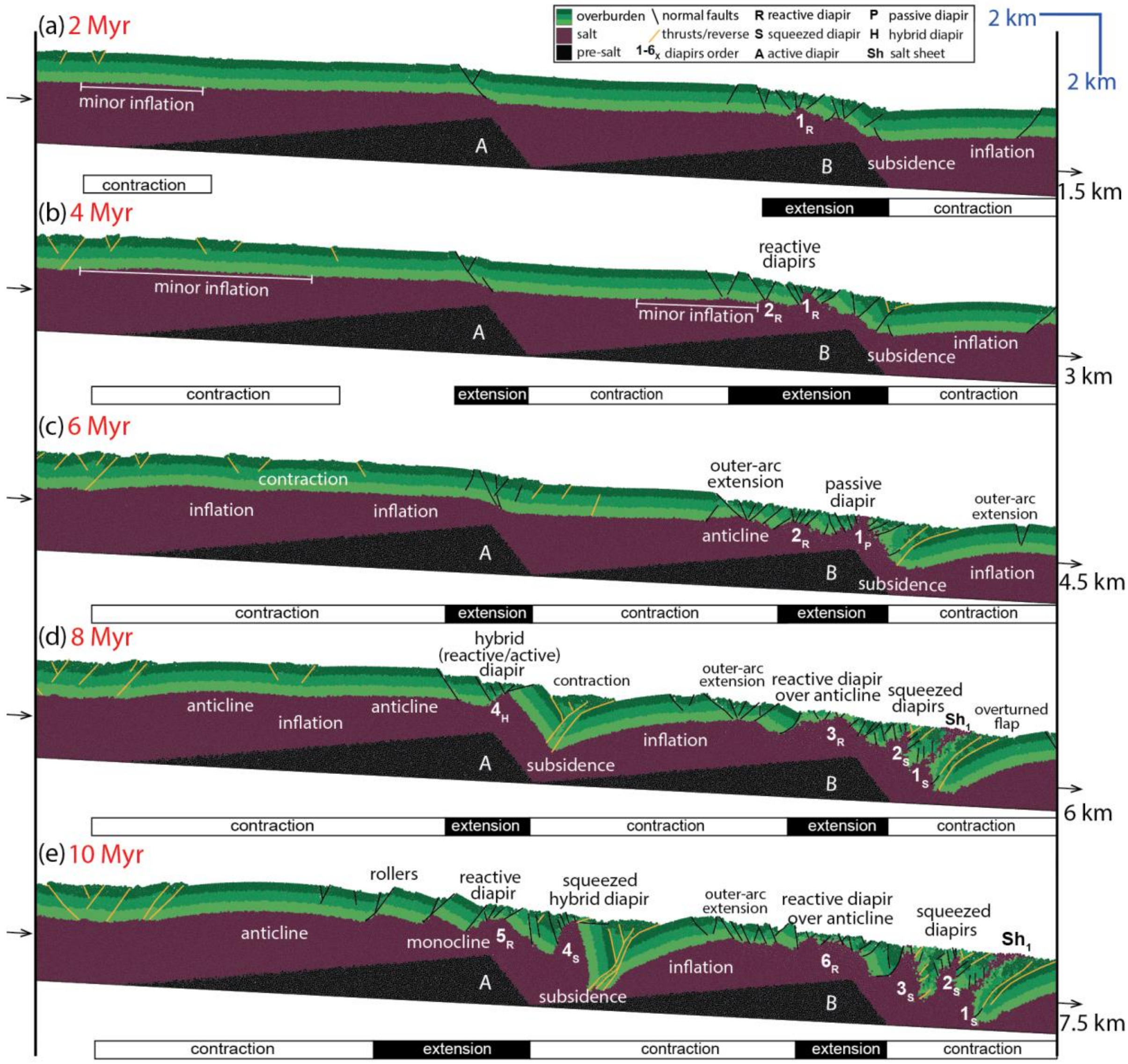

1051

1052 Figure 4

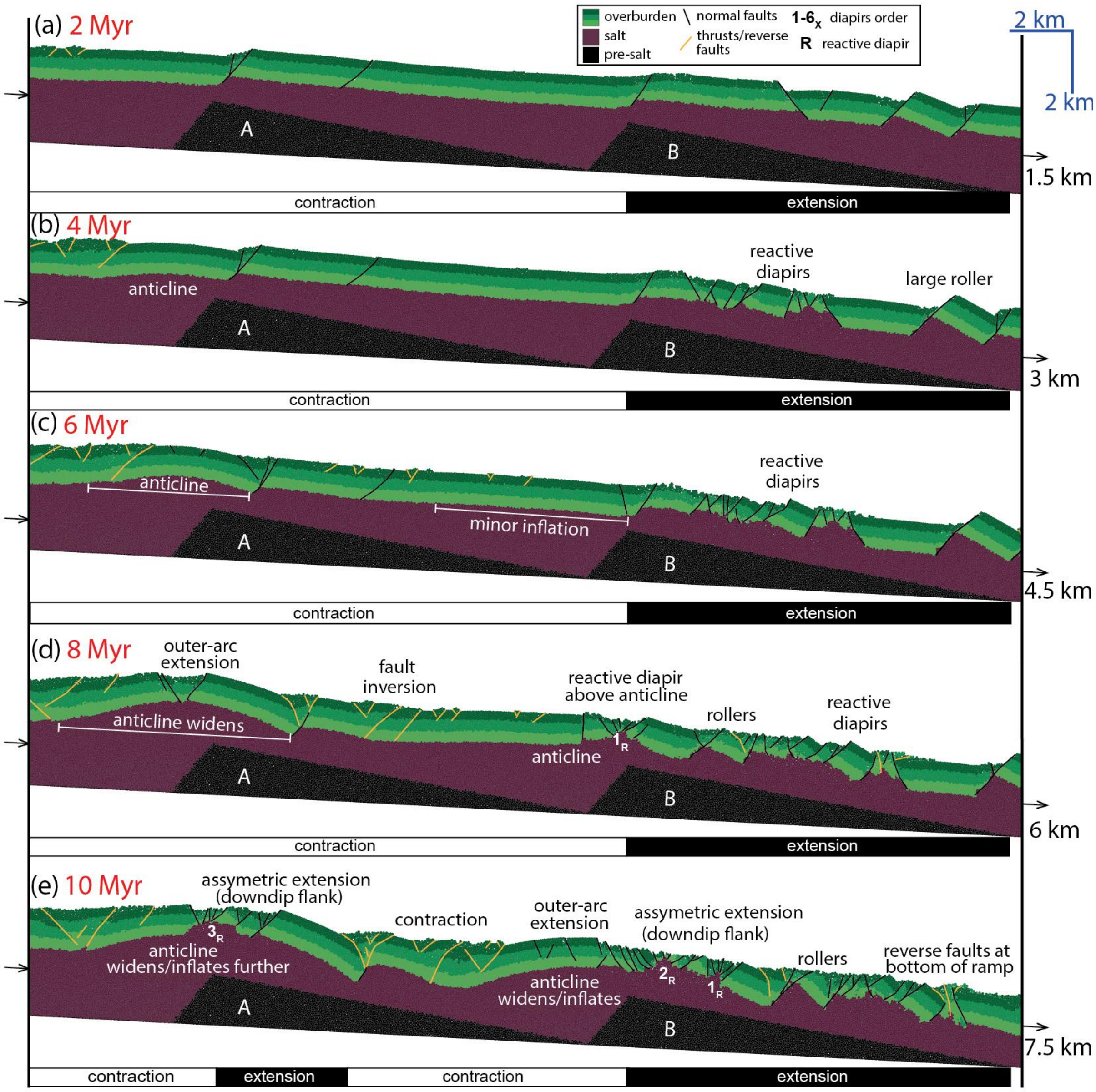

1053

1054 Figure 5

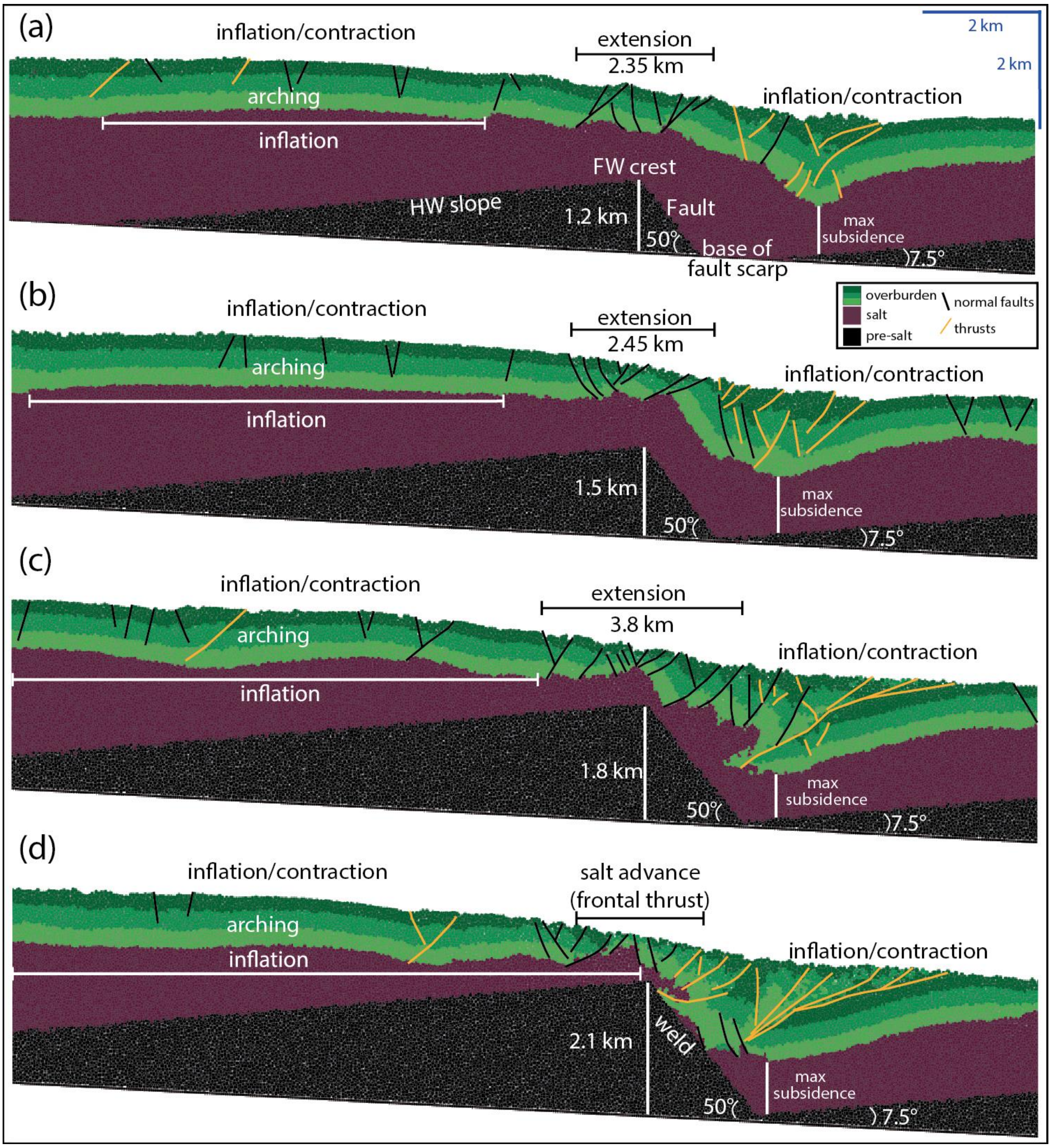

1055
1056 Figure 6

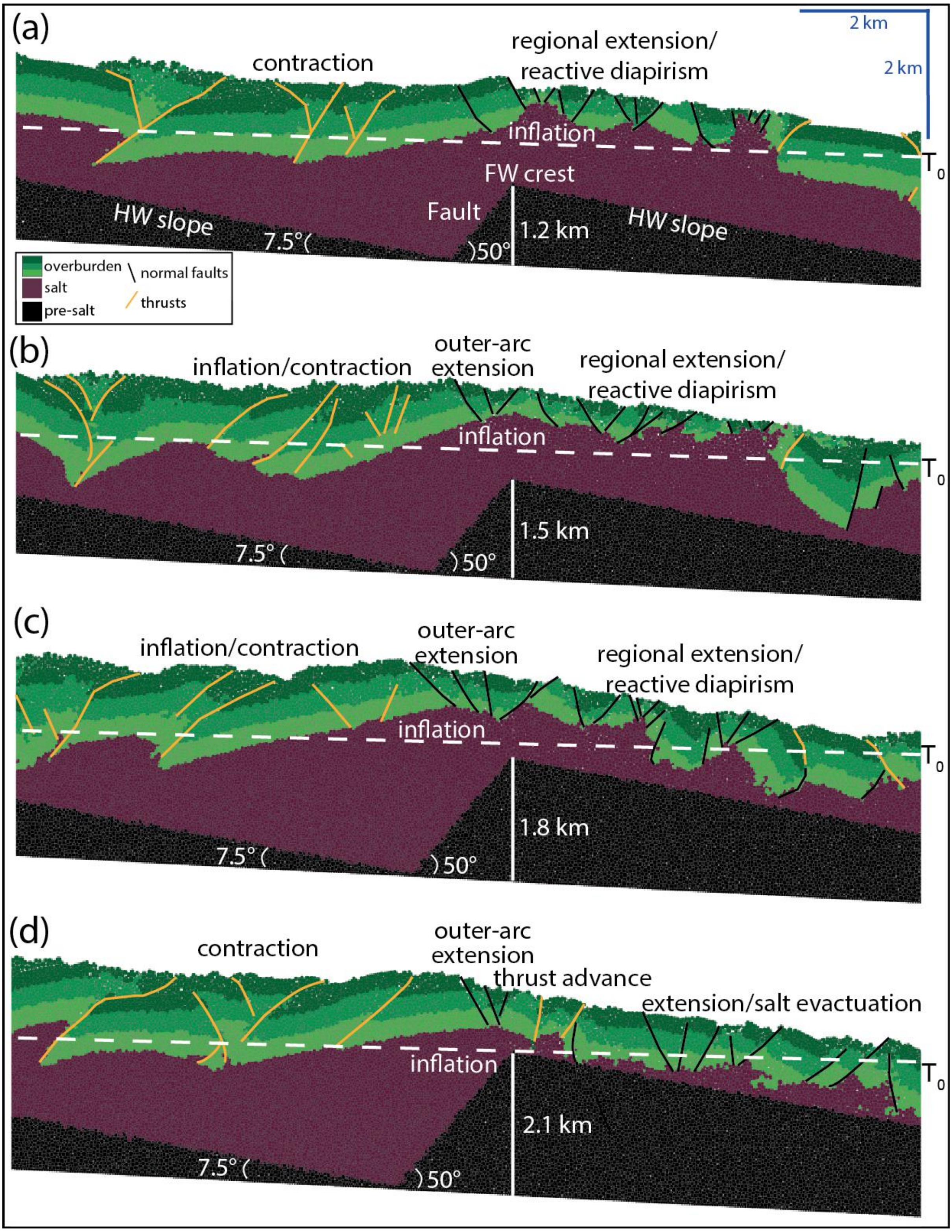

1057

1058 Figure 7

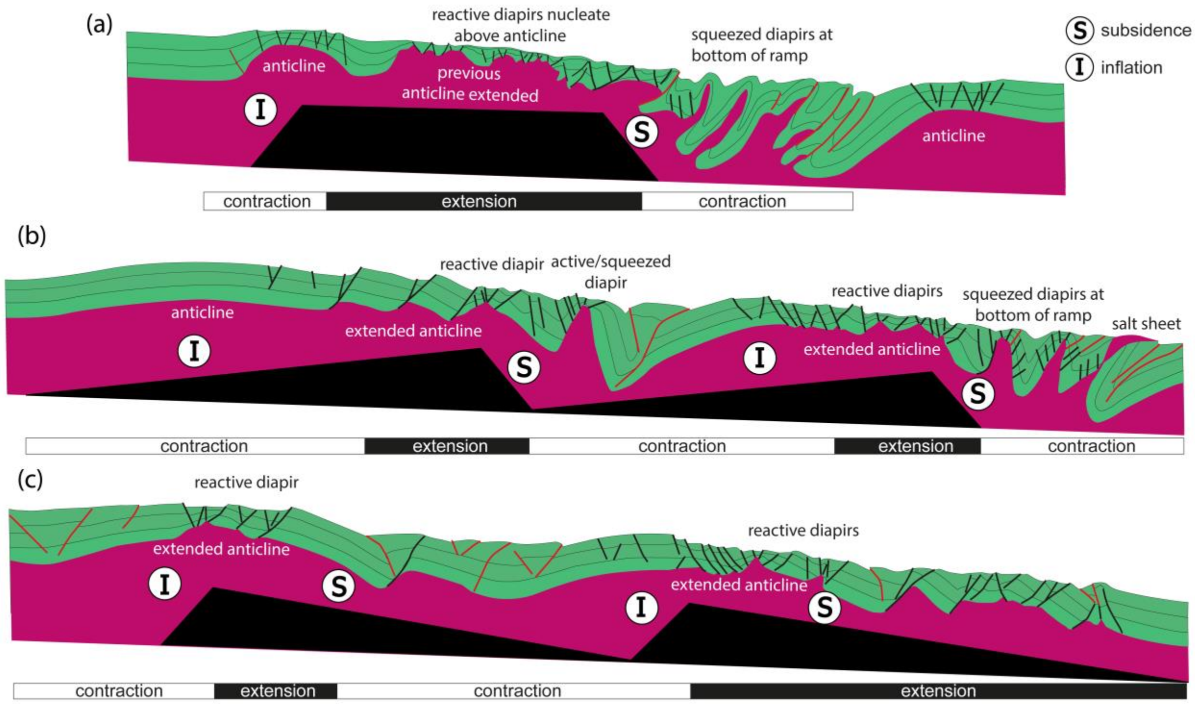
(a)
reactive diapirs nucleate above anticline
squeezed diapirs at bottom of ramp
S subsidence
I inflation
anticline
previous anticline extended
I
S
anticline
contraction
extension
contraction
(b)
reactive diapir
active/squeezed diapir
reactive diapirs
squeezed diapirs at bottom of ramp
salt sheet
anticline
extended anticline
I
S
I
extended anticline
S
contraction
extension
contraction
extension
contraction
(c)
reactive diapir
reactive diapirs
extended anticline
I
S
I
extended anticline
S
contraction
extension
contraction
extension

Figure 8

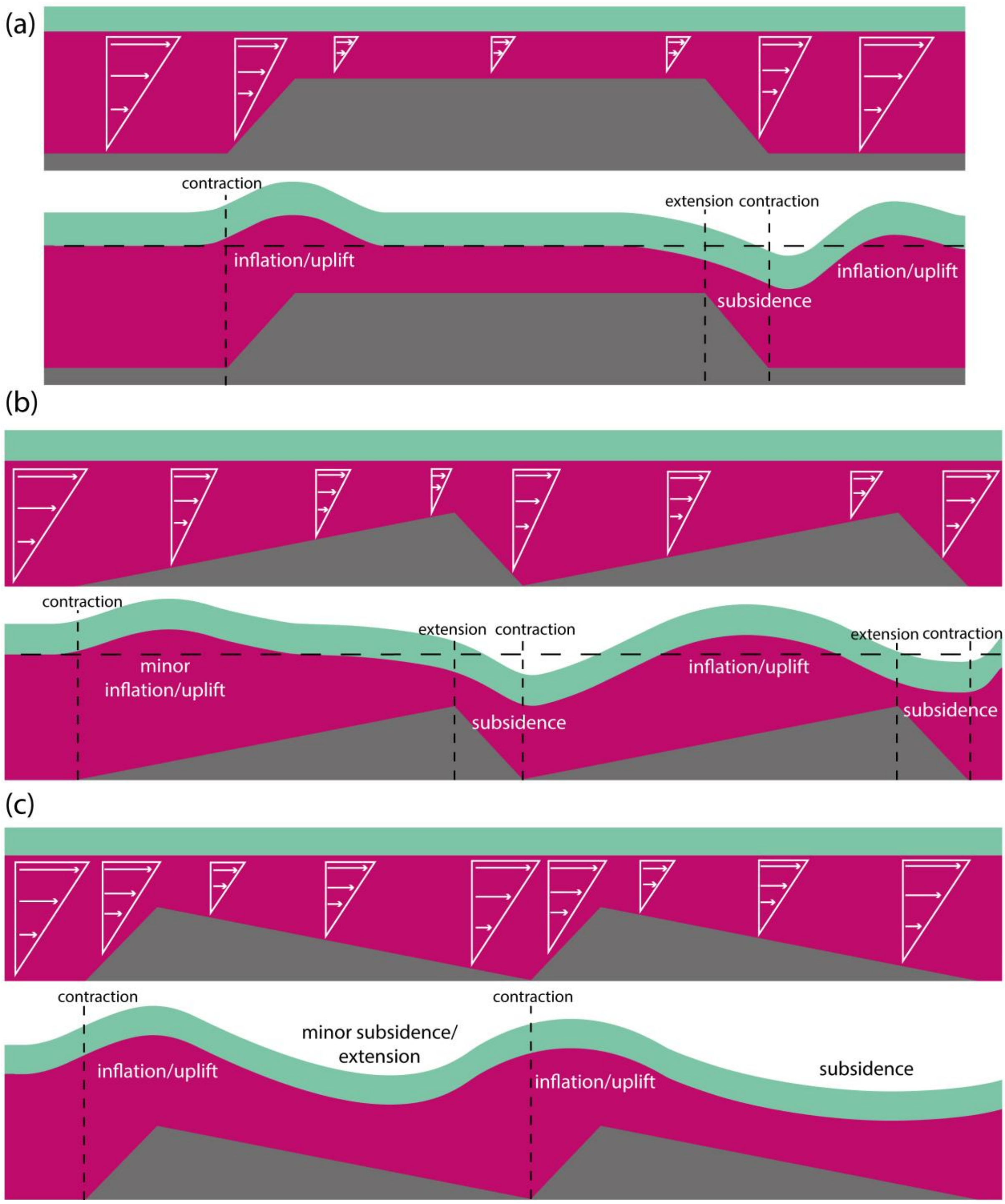

1061
1062 Figure 9

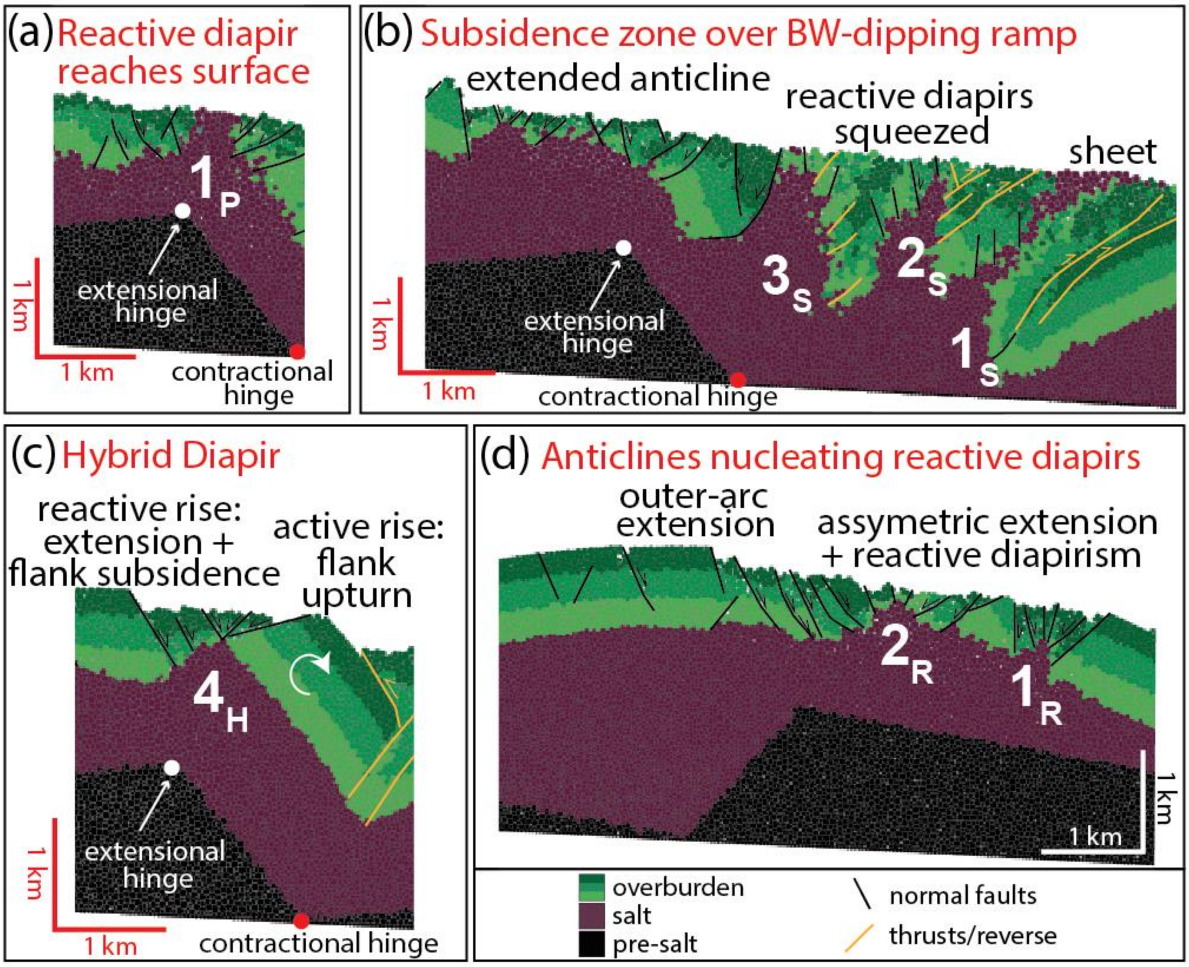

1063

1064 Figure 10

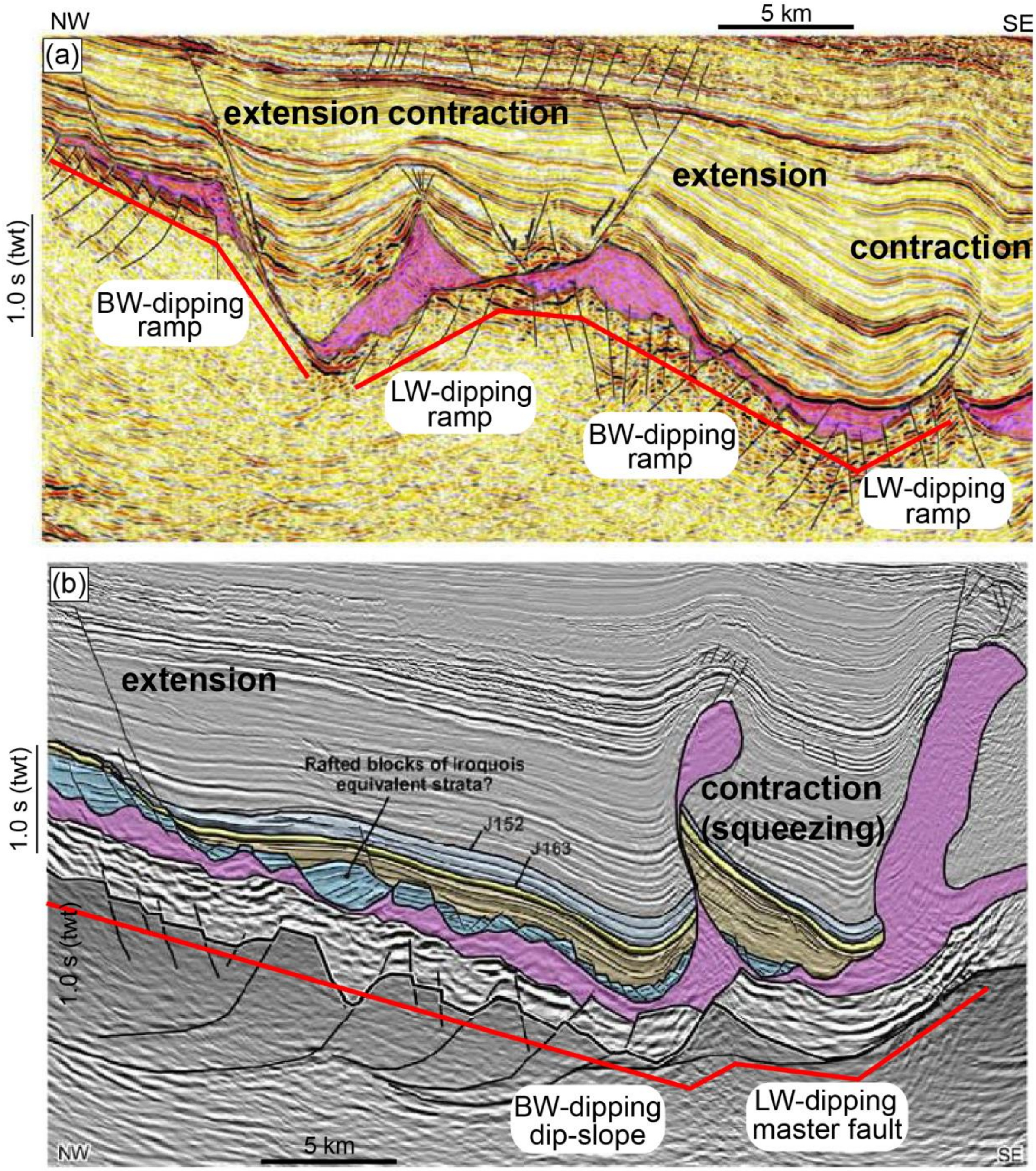
NW
5 km
SE
(a)
extension contraction
extension
contraction
1.0 s (twt)
BW-dipping ramp
LW-dipping ramp
BW-dipping ramp
LW-dipping ramp
(b)
extension
1.0 s (twt)
Rafted blocks of Iroquois equivalent strata?
J152
J163
contraction (squeezing)
1.0 s (twt)
BW-dipping dip-slope
LW-dipping master fault
NW
5 km
SE

Figure 11

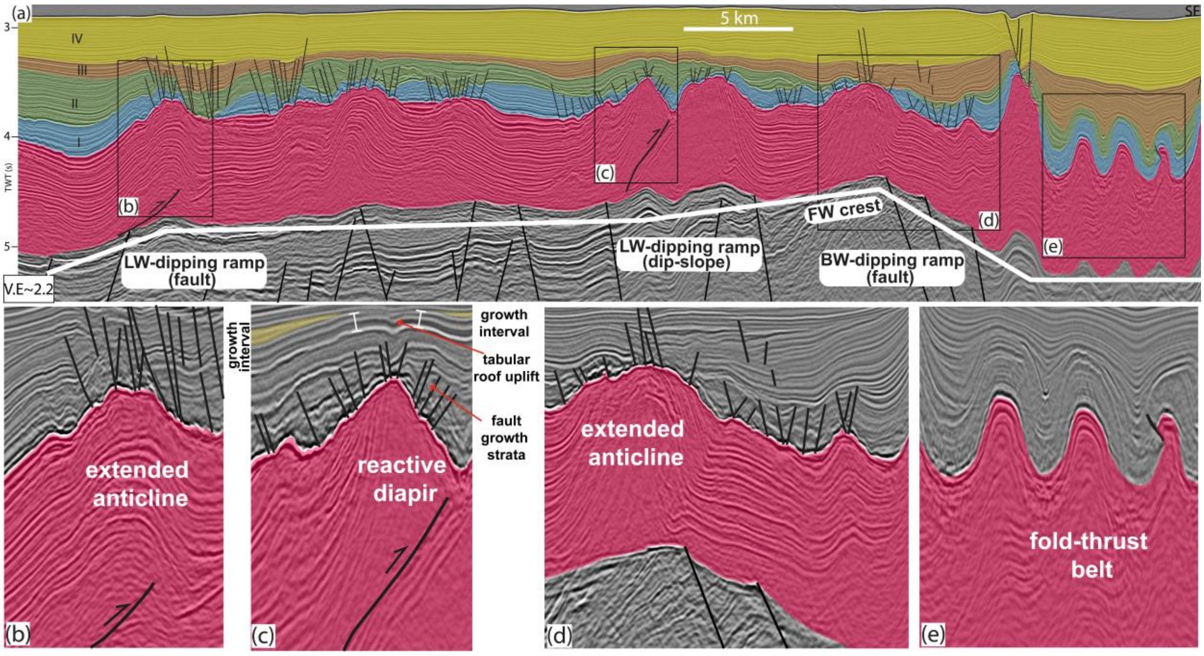

Figure 12

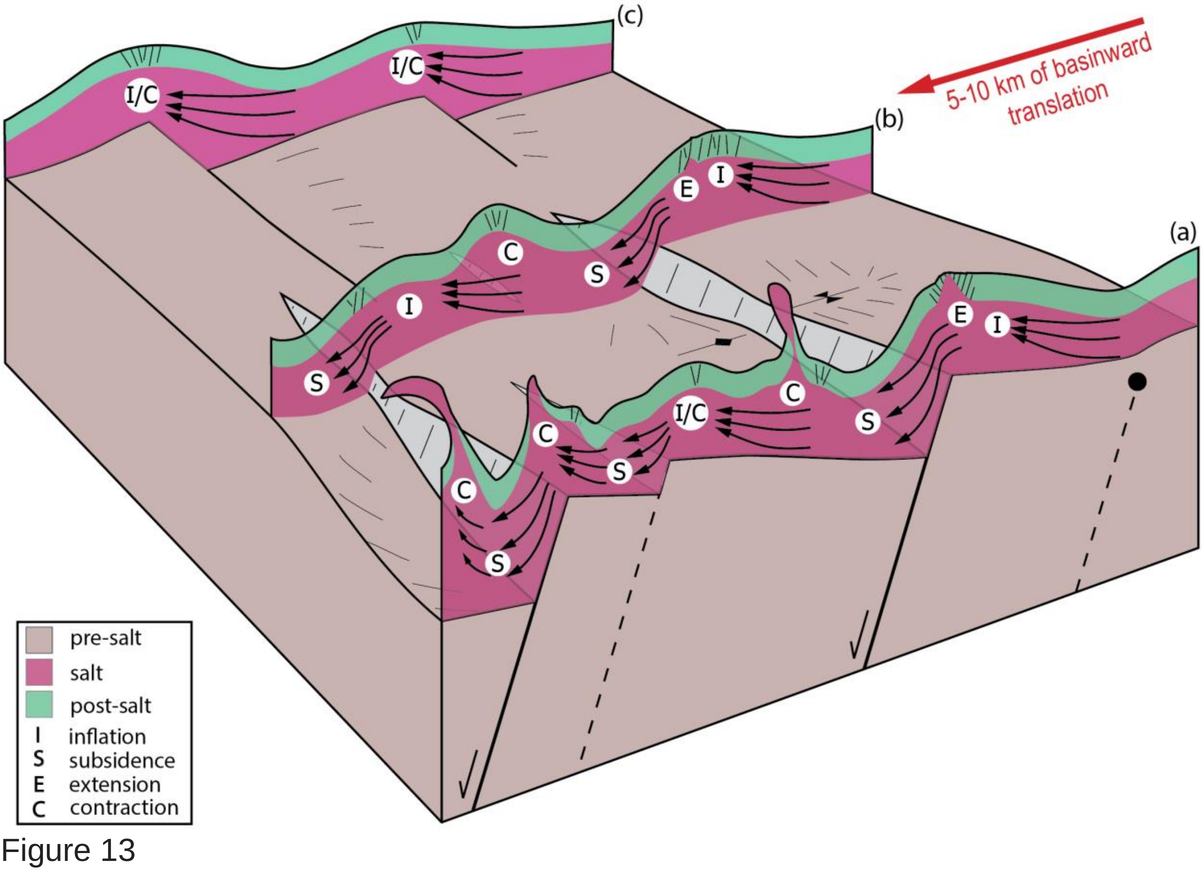

Figure 13

	pre-salt faults dip-direction	block length (km)	step height (km)	min salt thickness (km)
Model A	land and basinward	8	1.35	0.75
Model B	basinward	10	1.35	0.75
Model C	landward	10	1.35	0.75
Model B1	basinward	8.8	1.2	0.9
Model B2	basinward	11	1.5	0.6
Model B3	basinward	13.2	1.8	0.3
Model B4	basinward	15.4	2.1	0
Model C1	landward	8.8	1.2	0.9
Model C2	landward	11	1.5	0.6
Model C3	landward	13.2	1.8	0.3
Model C4	landward	15.4	2.1	0

Table 1